

Seismic scattering and absorption properties of Mars estimated through coda analysis on a long-period surface wave of S1222a marsquake

Keisuke Onodera¹, Takuto Maeda², Kiwamu Nishida³, Taichi Kawamura⁴, Ludovic Margerin⁵, Sabrina Menina⁶, Philippe H. Lognonne⁷, and William Bruce Banerdt⁸

¹The University of Tokyo

²Hirosaki University

³Earthquake Research Institute, University of Tokyo

⁴Université Paris Cité, Institute de physique de globe de Paris, CNRS

⁵Paul Sabatier University - Toulouse III

⁶Institut de Physique du Globe de Paris

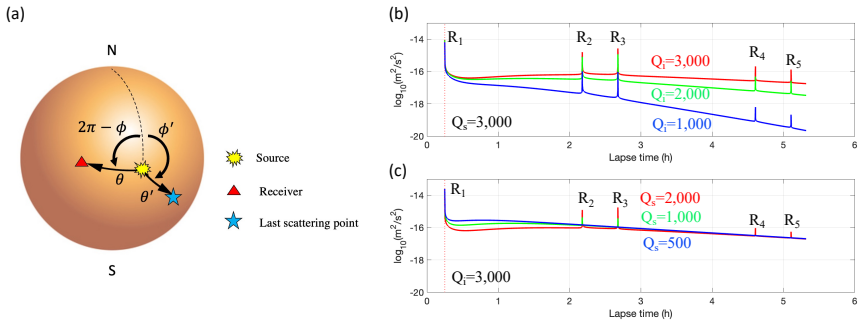
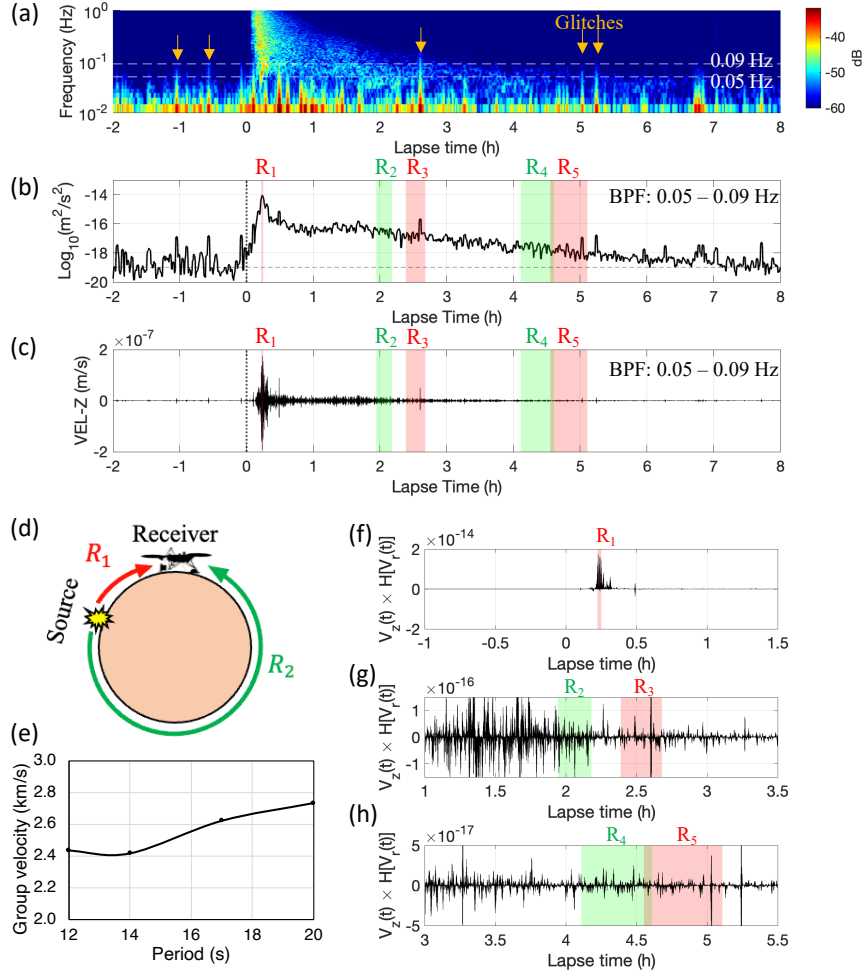
⁷Institut De Physique Du Globe De Paris

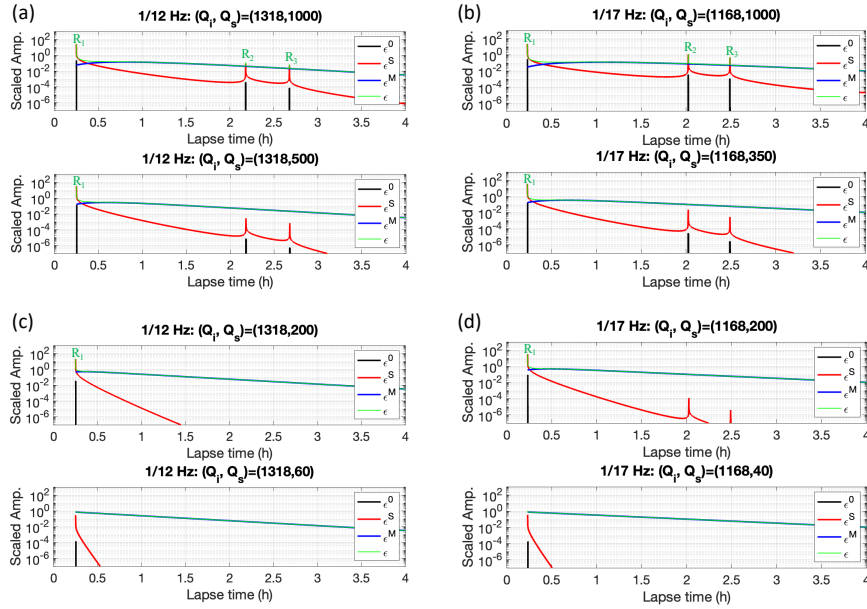
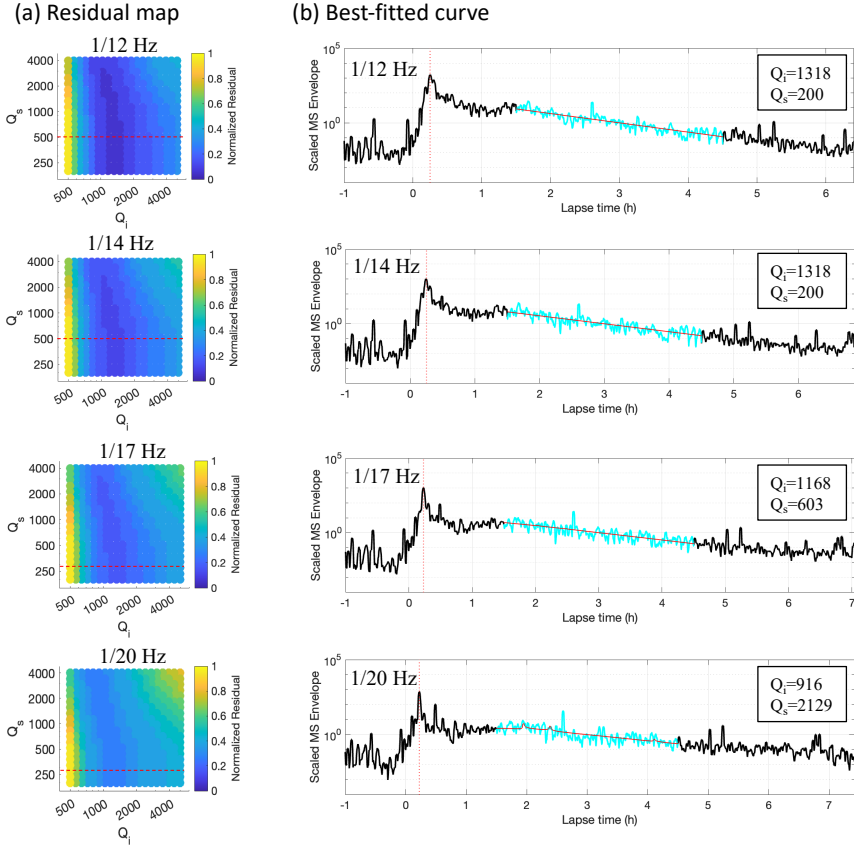
⁸Jet Propulsion Laboratory

January 20, 2023

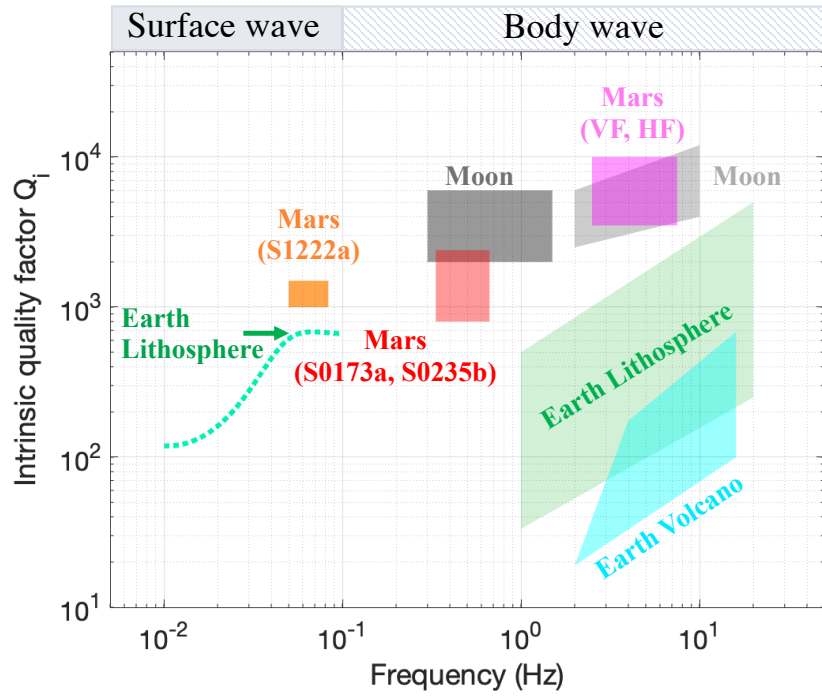
Abstract

On May 4th 2022, the seismometer on Mars observed the largest marsquake (S1222a) during its operation. One of the most specific features of S1222a is the long event duration lasting more than 8 hours from the occurrence, in addition to the clear appearance of body and surface waves. As demonstrated on Earth, by modeling a long-lasting and scattered surface wave with the radiative transfer theory, we estimated the scattering and intrinsic quality factors of Mars (Q_s and Q_i). This study especially focused on the frequency range between 0.05 - 0.09 Hz, where Q_s and Q_i have not been constrained yet. Our results revealed that $Q_i = 1000 - 1500$ and $Q_s = 30 - 500$. By summarizing the Martian Q_i and Q_s estimated so far and by comparing them with those of other celestial bodies, we found that, overall, the Martian scattering and absorption properties showed Earth-like values.

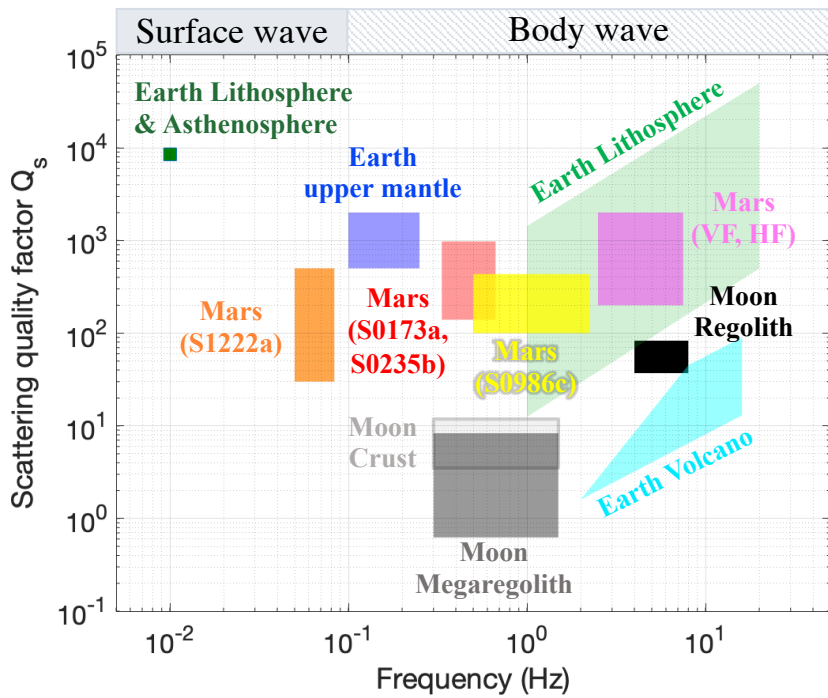




(a)



(b)



1 **Seismic scattering and absorption properties of Mars**
2 **estimated through coda analysis on a long-period**
3 **surface wave of S1222a marsquake**

4 **Keisuke Onodera¹, Takuto Maeda², Kiwamu Nishida¹, Taichi Kawamura³**
5 **Ludovic Margerin⁴, Sabrina Menina³, Philippe Lognonné³**
6 **William Bruce Barnedt⁵**

7 ¹Earthquake Research Institute, The University of Tokyo, Tokyo, Japan

8 ²Graduate School of Science and Technology, Hirosaki University, Hirosaki, Aomori, Japan

9 ³Université Paris Cité, Institut de Physique du Globe de Paris, CNRS, Paris, France

10 ⁴Institut de Recherche en Astrophysique et Planétologie, Université Toulouse III Paul Sabatier, CNRS,

11 CNES, Toulouse, France.

12 ⁵Jet Propulsion Laboratory, California Institute of Technology, California, USA

13 **Key Points:**

- 14 • We modeled the scattering effect of the largest marsquake (S1222a) using radia-
15 tive transfer theory on a spherical Mars.
16 • The inversion revealed that the intrinsic and scattering quality factors below 0.1
17 Hz were 1000 – 1500 and 30 – 500, respectively.
18 • We summarized the Martian quality factors derived so far and found that they
19 are relatively Earth-like rather than Moon-like.

Abstract

On May 4th 2022, the seismometer on Mars observed the largest marsquake (S1222a) during its operation. One of the most specific features of S1222a is the long event duration lasting more than 8 hours from the occurrence, in addition to the clear appearance of body and surface waves. As demonstrated on Earth, by modeling a long-lasting and scattered surface wave with the radiative transfer theory, we estimated the scattering and intrinsic quality factors of Mars (Q_s and Q_i). This study especially focused on the frequency range between 0.05 – 0.09 Hz, where Q_s and Q_i have not been constrained yet. Our results revealed that $Q_i = 1000 - 1500$ and $Q_s = 30 - 500$. By summarizing the Martian Q_i and Q_s estimated so far and by comparing them with those of other celestial bodies, we found that, overall, the Martian scattering and absorption properties showed Earth-like values.

Plain Language Summary

Since February 2019, NASA’s InSight (Interior Exploration using Seismic Investigations, Geodesy, and Heat Transport) has been conducting quasi-continuous seismic observation for more than three years. The seismic data from Mars has contributed significantly to a better understanding of the interior structure and the seismicity of the red planet. On May 4th 2022 (1222 Martian days after landing), another key event occurred, called S1222a. The event showed the largest seismic moment release (magnitude 4.7) and extremely long duration (> 8 hours) with intense seismic scattering. As demonstrated on Earth, the long-lasting scattered waves are useful for retrieving information about the structural heterogeneity within a planet. In this study, by applying the radiative transfer theory — which considers the energy transportation from the seismic source to the observation point — to Mars, we evaluated the energy decay rate due to seismic scattering and energy absorption by a medium. By comparing our results with those of other solid bodies, we found that the Martian scattering and absorption features were closer to the terrestrial ones than to the lunar ones.

1 Introduction

After almost three years of seismic observations on Mars, the seismometer installed by Interior Exploration using Seismic Investigations, Geodesy, and Heat Transport (InSight) detected a magnitude 4.7 class event on Sol 1222 (1222 Martian days after landing). Following the convention of Marsquake Service (MQS), this event was labeled as S1222a (Kawamura et al., 2022).

InSight deployed two types of seismometers: the Very Broadband seismometer (VBB) covering from a 0.01 – 10 Hz frequency band, and the Short-Period seismometer (SP) covering from 1 – 50 Hz [e.g., Lognonné et al. (2019)]. Quasi-continuous observations since 2019 brought us new insights into the Martian seismicity and internal structure [e.g., Lognonné et al. (2020); Banerdt et al. (2020); Giardini et al. (2020); Khan et al. (2021); Knapmeyer-Endrun et al. (2021); Stähler et al. (2021)].

As described by Kawamura et al. (2022), only VBB was operated on Sol 1222 due to the severe power supply conditions. That is, this event is only available for VBB (the channel names are XB.ELYSE.02.[BHU, BHV, and BHW], for instance). The remarkable characteristics of S1222a are, in addition to clear P- and S-wave arrivals, the excitation of both Rayleigh and Love waves, which are rarely observed in other marsquakes [Kawamura et al. (2022), Kim et al. (2022)]. Figures 1a-c show an example of the time series of S1222a. From top to bottom, followed by the spectrogram, the mean squared envelope (MS envelope), and the waveform filtered at 0.05 – 0.09 Hz are shown. Interestingly, the low-frequency energy lasts approximately 8 hours from the arrival (e.g., Figure 1b). The gradual decrease from the energy peak is called the coda. In terrestrial seis-

69 mology, it is known that the coda waves are generated due to the heterogeneous struc-
70 tures within a planet [e.g., Aki (1969); Aki and Chouet (1975)].

71 In this study, to constrain the scattering and attenuation properties of the Mar-
72 tian lithosphere, we focus on the decay coda part at a frequency of 0.05 – 0.09 Hz, where
73 Rayleigh wave is strongly excited, and the contamination of glitches is smaller than that
74 of lower frequencies (< 0.05 Hz). As these parameters have been poorly constrained at
75 that frequency, our study fills the missing piece regarding the heterogeneous structures
76 of Mars. Because the inhomogeneous structure of a planet strongly reflects the evolu-
77 tion processes in the past, understanding the heterogeneous structure would be one of
78 the paramount steps toward revealing the history of Mars.

79 In the following, we will review the Rayleigh wave features of S1222a, introduce how
80 to retrieve the scattering and attenuation parameters from the decay coda, and then show
81 the inversion results. Finally, we compare the intrinsic and scattering attenuation prop-
82 erties between the Earth, the Moon, and Mars.

83 2 The observed Rayleigh wave and its multi-orbital phases

84 In Figures 1b-c, the Rayleigh wave arrival (R_1), which was identified by Kawamura
85 et al. (2022), is shown by the red filled area. The expected arrival times of Rayleigh wave
86 traveling along the major arc (R_2) and the multi-orbital phases (R_3 , R_4 , and R_5) are
87 shown by the green and red-filled areas. See Figures 1d-e and the caption for the descrip-
88 tion of the multi-orbital phases of Rayleigh waves and their group velocity. At first glance,
89 the phases following R_1 are not clearly seen in our target frequency range. To confirm
90 whether such phases are present in the data, we performed a simple demonstration, as
91 described below.

92 If the Rayleigh wave component is excited, there must be a $\pi/2$ phase shift between
93 the vertical and radial seismic records. In other words, the multiplication of the verti-
94 cal ground velocity $V_z(t)$ and the Hilbert-transformed radial velocity $\mathcal{H}[V_r(t)]$ should re-
95 turn the one-sided signal during the arrival of the Rayleigh wave components (e.g., the
96 positive signal for R_1 , R_3 , R_5 and the negative signal for R_2 and R_4). Figure 1f shows
97 an example of Rayleigh wave detection. Around 0.2 h lapse time (R_1 arrival), the pos-
98 itive one-sided signal lasts for approximately 10 min, indicating that the Rayleigh wave
99 component arrives during this period. On the other hand, looking at Figures 1g-h, it is
100 difficult to find Rayleigh wave-related phases because of the low signal-to-noise ratio. In
101 other words, the scattering effect seems strong enough to attenuate both R_2 and the multi-
102 orbital phases to the level of other incoherent signals, at least in our target frequency
103 range (0.05 – 0.09 Hz). This is consistent with the report by Kawamura et al. (2022),
104 who could not confirm these phases in this frequency range, either.

105 3 Radiative transfer modeling on a spherical Mars

106 In terrestrial seismology, the radiative transfer theory has been used to investigate
107 the heterogeneous structures [e.g., Aki and Chouet (1975); Sato (1977); Wu (1985)]. Re-
108 cently, Menina et al. (2021) and Karakostas et al. (2021) applied this approach to Mars
109 and estimated the scattering and attenuation properties. To further advance our under-
110 standing of this topic, we will investigate the scattering and attenuation properties at
111 a lower frequency (< 0.1 Hz) than before, utilizing the scattering features observed in
112 S1222a.

113 In the following analysis, we consider a sphere with a Martian radius $R = 3389.5$
114 km on the spherical coordinate system, where the seismic source (S1222a) and a receiver
115 (InSight SEIS) are located on (3.0°S, 171.9°E) and (4.502°N, 135.623°E), respectively (Golombek
116 et al., 2020; Kawamura et al., 2022). From a source to receiver, the distance along the

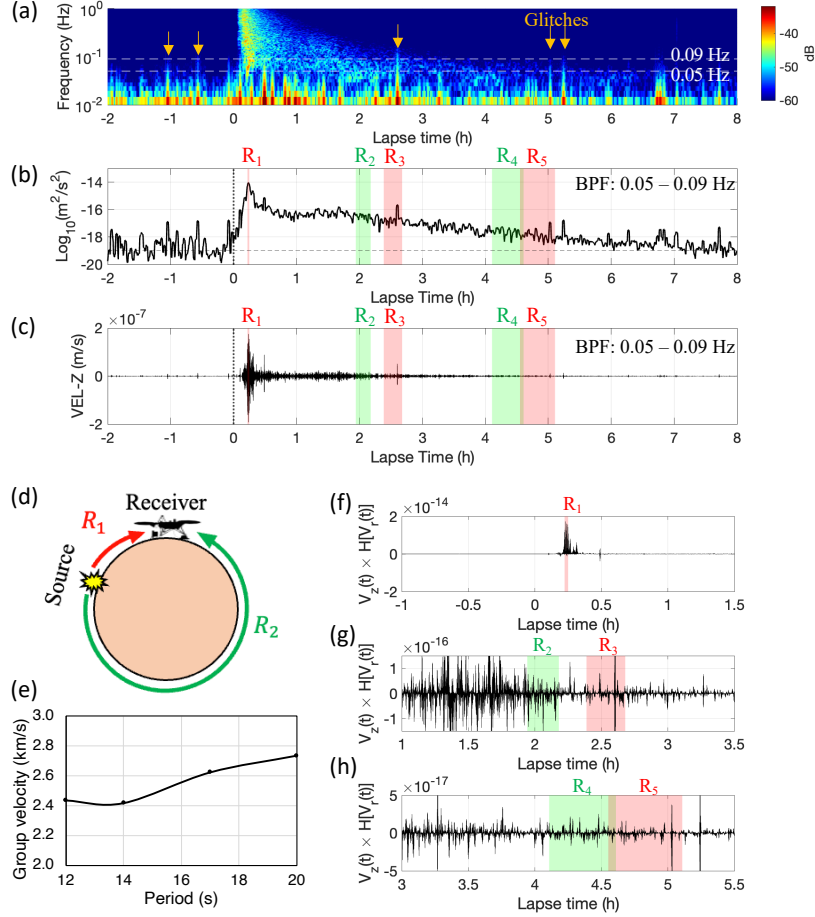


Figure 1. (a) Spectrogram of the VBB vertical component. The horizontal axis represents the lapse time in hours from the origin time, and the vertical axis shows frequency covering from 10^{-2} to 1 Hz. The orange arrows show the representative glitches seen in this time period. (b) Mean squared (MS) envelope at the low-frequency band. The deglitched waveform data (see the text) was bandpass filtered between 0.05 and 0.09 Hz, and the squared time series were smoothed with a time window of 100 s with 50% overlap. The red line tagged R_1 shows the R_1 arrival read by Kawamura et al. (2022). The red and green filled areas show the expected arrival times of the multi-orbital phases (R_2 , R_3 , ...), which are computed based on the group velocity shown in (e). The horizontal broken line shows the noise level estimated with the median value before the origin time, which is consistent with the representative noise level for this period of the sol (Figure S1). (c) The vertical-component waveform filtered between 0.05 and 0.09 Hz. The vertical lines and filled areas are the same as in (b). (d) Schematic diagram of Rayleigh wave propagation on a spherical Mars surface. R_1 refers to the Rayleigh wave propagating along the minor arc, and R_2 refers to that traveling along the major arc. The subscript number increases by two as the Rayleigh wave goes around Mars (i.e., R_3 , R_5 , ... for minor arc direction). (e) The dispersion curve for the group velocity as a function of period. (f)-(h) Time series of $V_z(t) \times \mathcal{H}[V_r(t)]$ at 0.05 – 0.09 Hz band for the time window of -1 – 1.5 h, 1 – 3.5 h, and 3 – 5.5 h lapse time, respectively. The red and green areas show the expected arrival times of Rayleigh wave components as in (b) and (c).

117 minor arc θ and the forward azimuth ϕ are measured as shown in Figure 2a. Accord-
 118 ing to Kawamura et al. (2022), $\theta = 37 \pm 1.6^\circ$ and $\phi = 281 \pm 11^\circ$. The last scattering
 119 point — where the seismic wave radiated from the source encounters before the arrival
 120 at the receiver — is apart from the source with the distance and the forward azimuth
 121 being θ' and ϕ' . Under this geometry setting, let us consider the energy density of the
 122 fundamental-mode Rayleigh wave for (i) the direct wave component, (ii) the single-scattered
 123 component, and (iii) the multiple-scattered component to model the observed MS en-
 124 velope.

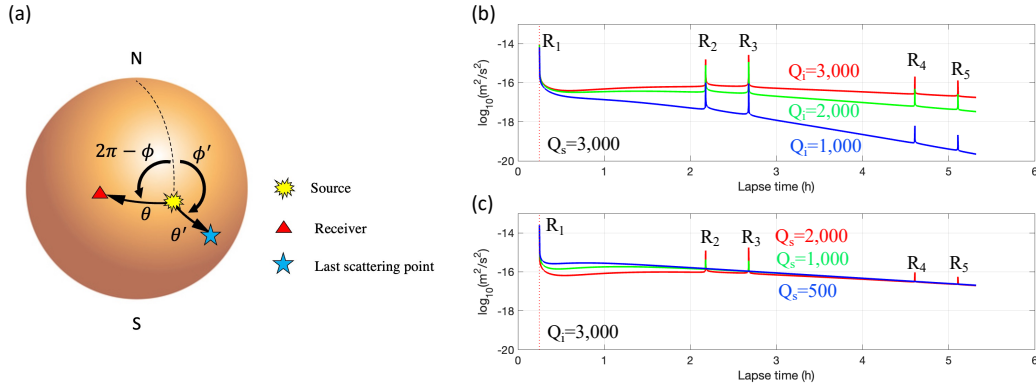


Figure 2. (a) Geometry of a source, receiver, and the last scattering point. (b) Comparison of theoretical MS envelopes for the different intrinsic quality factors ($Q_i=1000$, 2000, and 3000) with Q_s fixed to 3000. (c) Comparison of theoretical MS envelopes for the different scattering quality factors ($Q_s=500$, 1000, and 2000) with Q_i fixed to 3000.

125 Following Sato and Nohechi (2001), the energy density of Rayleigh waves propa-
 126 gating along the minor and major arcs on a spherical planet can be written as:

$$E^0(\theta, \phi, t) = \frac{W\Phi(\phi)}{2\pi R^2 \sin \theta} \sum_{n=0}^{\infty} \left[\delta \left(\frac{Vt}{R} - \theta - 2\pi n \right) + \delta \left(\frac{Vt}{R} + \theta - 2\pi(n+1) \right) \right], \quad (1)$$

127 where t is the time, W is the scaled energy factor, V is the group velocity, and δ is the
 128 delta function. Φ denotes the radiation pattern of the source. Because of the large un-
 129 certainty in the focal mechanism with a single-spot observation, we assumed the isotropic
 130 radiation for Φ as:

$$\Phi = \frac{1}{2\pi}. \quad (2)$$

131 Normalizing the energy density with $W/4\pi R^2$ and introducing the intrinsic and scatter-
 132 ing attenuation factors yields the scaled energy density of the direct wave component ϵ^0 :

$$\epsilon^0(\theta, t; \omega) = \frac{2\Phi}{\sin \theta} \sum_{n=0}^{\infty} \left[\delta \left(\frac{Vt}{R} - \theta - 2\pi n \right) + \delta \left(\frac{Vt}{R} + \theta - 2\pi(n+1) \right) \right] e^{-(Q_s^{-1} + Q_i^{-1})\omega t}, \quad (3)$$

133 where ω is the angular frequency, and Q_s and Q_i are the scattering and intrinsic atten-
 134 uation factors, respectively.

135 As demonstrated for earthquakes (Sato & Nohechi, 2001; Sato & Nishino, 2002; Maeda
 136 et al., 2006), the energy density of single-scattered Rayleigh wave ϵ^S can be expressed
 137 as:

$$\epsilon^S(\theta, \phi, t; \omega) = \frac{\omega R}{\pi V Q_s} e^{-(Q_s^{-1} + Q_i^{-1})\omega t} \int_0^{2\pi} d\phi' \frac{\Phi n_s(\theta, t)}{\sqrt{(\sin \tau - \sin \theta \cos(\phi - \phi'))^2 + (\cos \theta - \cos \tau)^2}}, \quad (4)$$

138 where $\tau = Vt/R$, and the multiple orbit factor n_s is given by:

$$n_s(\theta, t) = \begin{cases} 0 & (\tau < \theta), \\ 1 & (\theta < \tau < 2\pi - \theta), \\ 2 & (2\pi - \theta < \tau < 2\pi + \theta), \\ 3 & (2\pi + \theta < \tau < 4\pi - \theta), \\ 4 & (4\pi - \theta < \tau < 4\pi + \theta), \\ \dots & \dots \end{cases} \quad (5)$$

139 To calculate the multiple scattering term, we use the asymptotic form, which has
 140 been validated as a good approximation for earthquakes (Sato & Nishino, 2002). The
 141 energy density of the multiple scattering term ϵ^M can be written as:

$$\epsilon^M(t; \omega) = \left(1 - e^{-\frac{\omega t}{Q_i}} - \frac{\omega t}{Q_s} e^{-\frac{\omega t}{Q_s}} \right) e^{-\frac{\omega t}{Q_i}}. \quad (6)$$

142 By combining all three terms above, we can theoretically draw the MS envelopes
 143 as follows:

$$E(\theta, \phi, t; \omega) = \frac{W}{4\pi R^2} [\epsilon^0(\theta, t; \omega) + \epsilon^S(\theta, \phi, t; \omega) + \epsilon^M(t; \omega)]. \quad (7)$$

144 Because the scaled energy factor W is unknown, we focus on the relative (or normalized)
 145 MS envelope and first evaluate the intrinsic and scattering quality factors, and then estimate
 146 W using the preferable quality factors (See Sections 5 and 6).

147 To clarify how Q_i and Q_s affect the envelope shape, Figures 2b-c show examples
 148 of the theoretical envelopes. Q_i mostly controls the energy decay rate, and Q_s determines
 149 the peak intensity of Rayleigh waves.

150 4 Target frequencies and data processing

151 We limit ourselves to studying the frequency range below 0.1 Hz, where the scat-
 152 tering and intrinsic quality factors have not been constrained yet. Especially we processed
 153 the data at the four frequencies: 1/12, 1/14, 1/17, and 1/20 Hz.

154 To reduce the contamination by glitches, we used the data denoised with the method
 155 proposed by Scholz et al. (2020). For preprocessing, we performed (i) detrending and de-
 156 meaning, (ii) applying pre-filtering between 0.005 and 9.5 Hz, and (iii) correcting the in-
 157 strumental response to convert the raw data into particle velocity. Then, the time trace
 158 was bandpass filtered using the 4th order Butterworth filter with the corner frequencies
 159 of $0.9f_c$ and $1.1f_c$, where f_c is the center frequency (1/12, 1/14, 1/17, and 1/20 Hz). As
 160 we focus on Rayleigh wave and stand on the approach by Sato and Nishino (2002), we
 161 used the vertical component of VBB in the analysis.

162 5 Inversion with grid search method

163 In the inversion process, we used the MS envelope normalized with an average value
 164 between 1.5 and 3.5 h lapse time for the respective frequency bands. In other words, we
 165 modeled the relative decay trend to obtain the scattering and intrinsic quality factors.

166 A grid search concerning the scattering quality factor Q_s and the intrinsic qual-
 167 ity factor Q_i was conducted. We varied the Q_s and Q_i in a range of 200 – 4000 and 500
 168 – 5000, respectively. The parameter ranges were equally divided into 20 on a log scale.
 169 The goodness of fit was evaluated with the summation of squared residual value σ , as
 170 follows:

$$\sigma_{j,k}(f_c) = \sum_{t_{min}}^{t_{max}} \left[\log_{10} \left(\frac{S^{obs}(t; f_c)}{S_{j,k}^{rtf}(t; f_c)} \right) \right]^2, \quad (8)$$

171 where t_{min} (= 1.5 h) and t_{max} (= 3.5 h) define the time window for the fitting, S^{obs} and
 172 S^{rtf} are the MS envelopes for the observation and the theoretical curve (scaled with the
 173 average value in the time window). The subscripts j and k in Equation 8 are for the varied
 174 Q_i and Q_s parameters. When $j = 1$ and $k = 1$, $Q_i = 500$ and $Q_s = 200$.

175 6 Estimated intrinsic and scattering quality factors and scaled energy 176 factor

177 Figure 3a presents the inversion results for the respective frequencies. The color
 178 map indicates the distribution of the residual values in the Q_i - Q_s parameter space, where
 179 the blue color indicates smaller residual values. Figure 3b displays the best-fitted curves
 180 for each frequency band (all calculated curves can be found in Figure S2). Looking at
 181 the residual map, Q_i is well constrained, whereas any Q_s can provide good fits as long
 182 as Q_i is in the range of 1000 – 1500. As demonstrated in Figures 2b-c, Q_i mostly con-
 183 trols the gradient of the decay coda, whereas Q_s affects the peak intensity of Rayleigh
 184 wave and its multi-orbital phases. Thus, it is reasonable that Q_i is more easily constrained
 185 than Q_s .

186 To better constrain Q_s , we performed an additional analysis considering that R_2
 187 and the multi-orbital phases were attenuated and could not be confirmed within our tar-
 188 get frequency range (Section 2). Figure 4 shows the examples of parameter studies on
 189 Q_s with Q_i fixed to the best-fitted value in the previous inversion. In Figures 4a-b, com-
 190 paring the first and the second rows gives us the upper limit of Q_s , which provides the
 191 smallest scattering intensity to hide the peaks of R_2 and the multi-orbital phases under
 192 the multiple scattering effects. In turn, Figures 4c-d provides us with the lower limit of
 193 Q_s which is the smallest scattering intensity to diffuse the R_1 peak completely. Conse-
 194 quently, we found that Q_s ranged from 60 to 500 for 1/12 and 1/14 Hz and from 30 to
 195 350 for 1/17 and 1/20 Hz, respectively (Figure 4 and Figure S3). It appears that Q_s de-
 196 pends on the frequency. However, this cannot be concluded because both Q_s -ranges re-
 197 turn similar residual values. Therefore, we conclude that the plausible Q_s range is 30 –
 198 500.

199 Together with the estimated Q_i and Q_s , we evaluated the scaled energy factor W .
 200 As shown in Figure S4, we calculated the summation of residual for each frequency band
 201 in the same manner as in Equation 8 and found a preferable W value of $(8.5 \pm 1.5) \times$
 202 $10^{-9} \text{ (m/s)}^2 \cdot \text{km}^2$.

203 7 Intrinsic and scattering quality factors of the Earth, the Moon, and 204 Mars

205 In this section, to compare the scattering and attenuation properties with the same
 206 criteria between the Earth, the Moon, and Mars, we review Q_i and Q_s derived thus far
 207 on each body. If previous studies provided different parameters, such as diffusivity or
 208 correlation length, we converted them into Q_i and Q_s . Because of a large uncertainty
 209 in the depth and thickness of the Martian scattering layer, a detailed discussion of the
 210 structures cannot be put forward. Instead, we limit ourselves to showing the compar-
 211 ative figures for Q_i and Q_s against frequency and giving a preliminary interpretation.

212 7.1 Earth

213 Figures 5a-b show the intrinsic and scattering quality factors for the Earth, the Moon,
 214 and Mars, respectively, where the quality factors for body waves are displayed above 0.1
 215 Hz, and those for surface waves are presented below 0.1 Hz.

216 The Earth's lithosphere Q_i and Q_s are estimated through the radiative transfer the-
 217 ory for isotropic single and/or multiple scattering models, using S-wave scattered waves

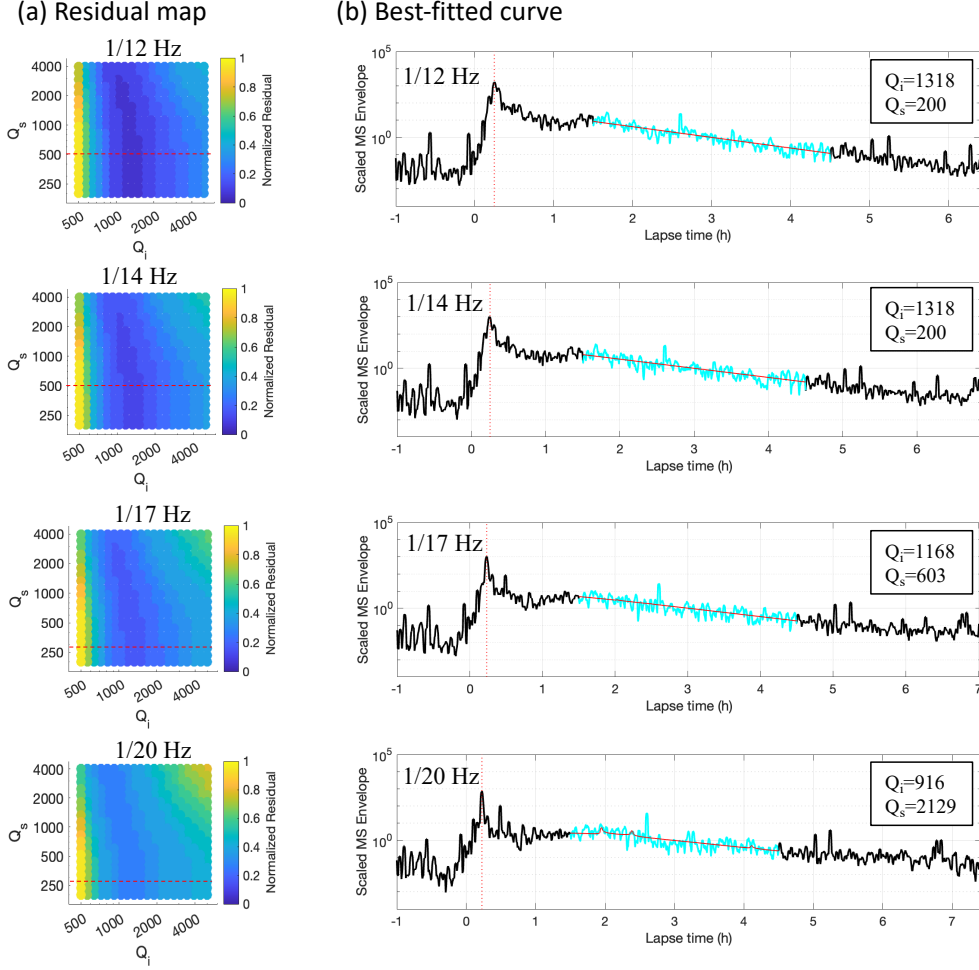


Figure 3. (a) Grid search results for the respective frequency bands (1/12 Hz through 1/20 Hz from the top to bottom). The horizontal axis shows the intrinsic Q_i , and the vertical axis shows the scattering Q_s . The color map represents the summation of the squared residual (Equation 8), which is normalized with the maximum value. The red dashed line shows the upper limit of the scattering Q_s (See the text for the details). (b) The best-fitted curves superposed on the observations. For the fitting, the cyan profiles (1.5 – 4.5 h window) were used out of the entire MS envelopes. The amplitude is normalized with the average value within the time window of 1.5 – 4.5 h. The red profiles show the best-fitted curves. Note that the theoretical curves in red were move averaged in the same way as the observation in black.

218 of local earthquakes. The lithosphere’s Q_i and Q_s for body waves in Figures 5a-b were
 219 taken from the recent reviews by Sato et al. (2012) and Sato (2019). Both quality factors
 220 show frequency dependence. Q_i ranges 30 – 500 at 2 Hz and 250 – 5000 at 20 Hz.
 221 Q_i for surface waves was computed using Mineos [Masters et al. (2011)] with the Pre-
 222 liminary Earth model [PREM; Dziewonski and Anderson (1981)]. The upper limit (\sim
 223 900) corresponds to the lithosphere. The value decreases with decreasing frequency be-
 224 cause Rayleigh wave at a lower frequency becomes more sensitive to the deeper part: the
 225 asthenospheric structure. The Q_s at 0.01 Hz (\sim 10000) was estimated by Sato and No-
 226 hechi (2001) analyzing the Rayleigh wave and its multiple orbits as performed in this
 227 study.

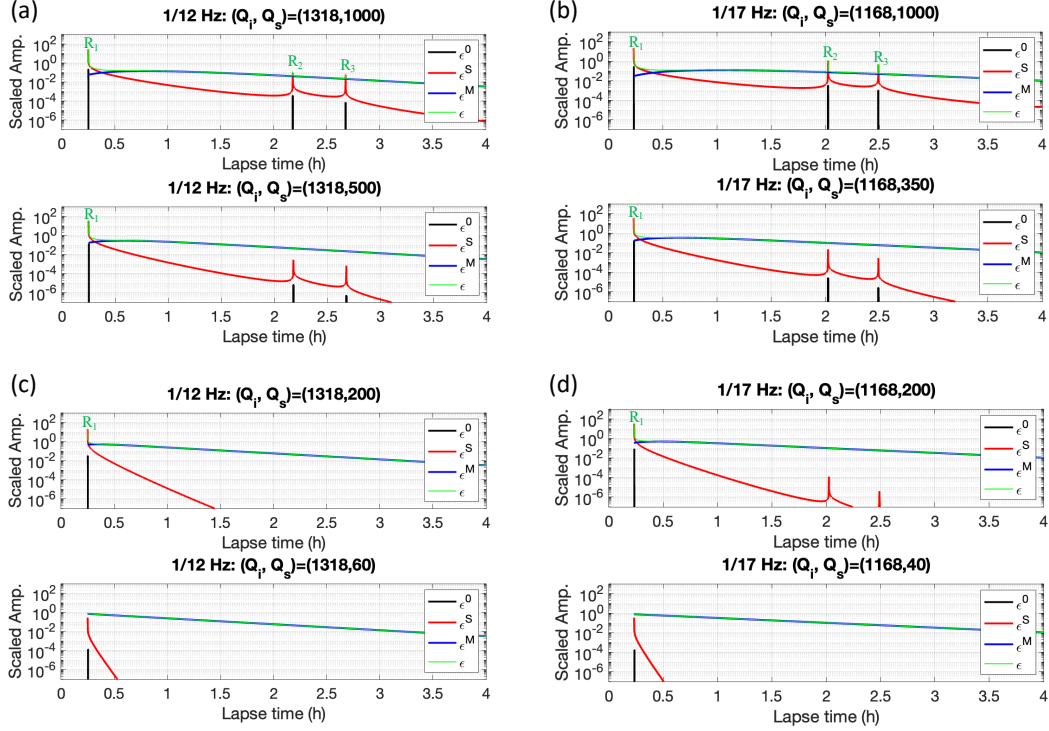


Figure 4. (a)-(b) Examples of parameter study results for estimating the upper limit of Q_s at 1/12 Hz and 1/17 Hz. The black lines are the direct wave component, the red profile is the single-scattered component, the blue is the multiple-scattered component, and the green is the convolved profile. The first row is for $Q_s = 1000$, where the multi-orbital phases can be seen. The second row is the case for the upper limit of Q_s , where the contribution of the multiple scattering is strong enough to bury R_2 and the multi-orbital phases. (c)-(d) Examples of parameter study results for estimating the lower limit of Q_s at 1/12 Hz and 1/17 Hz. The first row is for $Q_s = 200$, where the R_1 phase can be confirmed. The second row is the case for the lower limit of Q_s , where the contribution of the multiple scattering is strong enough to bury the R_1 phase.

228 Lee et al. (2003) and Lee et al. (2006) estimated the terrestrial mantle Q_s using
 229 ScS wave scattering. They inverted for the Q_s using the Monte Carlo method based on
 230 the radiative transfer theory with the PREM's velocity and attenuation structure. Around
 231 0.1 – 0.2 Hz in Figure 5b, we plotted the upper mantle value compatible with the up-
 232 per limit of the lithospheric value at 1 Hz.

233 The volcanic region is known to be one of the most heterogeneous regions on Earth.
 234 Previous studies evaluated the scattering parameters in various volcanic areas using body
 235 waves generated by artificial seismic sources. For example, Wegler (2003) evaluated the
 236 Q_i and Q_s at Vesuvius volcano in Italy, Yamamoto and Sato (2010) assessed the qual-
 237 ity factors at Asama volcano in Japan, and Prudencio et al. (2015) investigated Strom-
 238 boli volcano in Italy. The complied parameter ranges are shown as the cyan areas in Fig-
 239 ures 5a-b. When compared with the lithosphere, the volcanic area shows the smaller Q_i
 240 and Q_s , indicating the strong scattering and high attenuation rate.

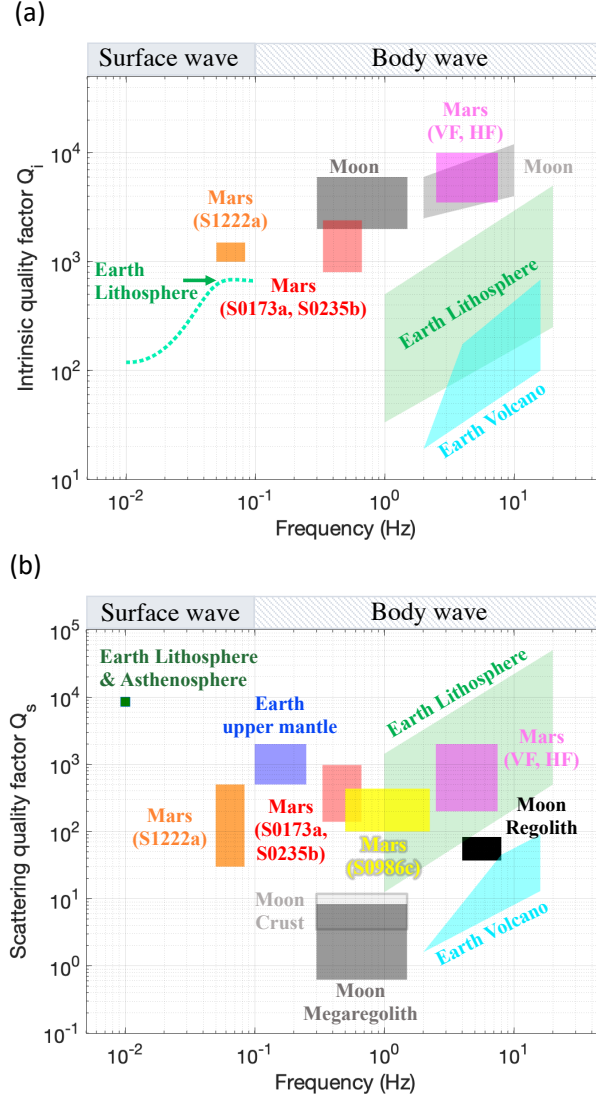


Figure 5. Comparison of (a) intrinsic quality factor and (b) scattering quality factor between the Earth, the Moon, and Mars. See Section 7 for the details.

241

7.2 Moon

242

The latest lunar intrinsic and scattering quality factors were evaluated by Blanchette-Guertin et al. (2012), Gillet et al. (2017), and Onodera et al. (2022).

243

244

Blanchette-Guertin et al. (2012) investigated the energy decay of the various types of moonquakes (such as deep moonquakes, shallow moonquakes, natural impacts, and artificial impacts) at different frequency bands, and systematically assessed the decay time and coda Q (Q_c). Under the intense scattering conditions, Q_c can be regarded as the S-wave Q_i [e.g., Yoshimoto and Jin (2008)]. In this study, assuming their Q_c estimation as Q_i , we show the corresponding Q_i range as dark and light grey areas in Figure 5a. The Q_i ranges from 2000 to 6000 in the middle frequency (0.3 – 1.5 Hz). Moreover, Q_i in the high frequency (2 – 10 Hz) takes a value of 2500 – 6000 at 2 Hz and 4000 – 12000 at 10 Hz, showing frequency dependence.

250

251

252

Regarding the scattering quality factors (black and grey areas in Figure 5b), Gillet et al. (2017) estimated the global Q_s by introducing the spherically layered geometry in the diffusion model. In Figure 5b, the crustal value (3.5 – 12) is presented as the light grey area. Nakamura (1976) evaluated the diffusivity of the regolith (surface fine and porous layer) as $(6.2 \pm 0.2) \times 10^{-3} \text{ km}^2/\text{s}$. It should be noted that we divided his estimation by 4 because the diffusivity in Nakamura (1976) was defined differently from that ordinarily used. Using the corrected diffusivity, we estimated the regolith's Q_s as 37 – 83 at 4 – 8 Hz (the black region in Figure 5b). For the megaregolith — the fractured structure due to continuous meteoroid impacts, Onodera et al. (2022) evaluated $Q_s = 0.6 – 8.3$ in the middle frequency (the dark grey area in Figure 5b) in a forward approach using full 3D seismic wave propagation simulation.

7.3 Mars

The initial estimation of the diffusivity and intrinsic attenuation were carried out by Lognonné et al. (2020) using both teleseismic events (S0173a and S0235b) and a regional marsquake (S0128a). As the results for S0128a are integrated with those of Menina et al. (2021), we briefly review the scattering parameters for S0173a and S0235b. Based on the radiative transfer modeling proposed by Margerin (2017), Lognonné et al. (2020) investigated the two teleseismic events. They estimated the diffusivity (200 – 700) and intrinsic quality factor (800 – 2400) at around 0.5 Hz. Here, we converted the diffusivity into the scattering Q (140 – 977). The red areas in Figures 5a-b correspond to their estimations.

Following the initial outcomes by Lognonné et al. (2020), Menina et al. (2021) evaluated the scattering and attenuation properties at higher frequencies (> 2.4 Hz) using Very High Frequency (VF) and High Frequency (HF) events. They took over the approach of Lognonné et al. (2020) and estimated Q_i and Q_s as 3500 – 10000 and 200 – 2000, respectively (the magenta areas in Figures 5a-b). Recently, using the seismic waves generated by a meteoroid impact (S0986c), Garcia et al. (2022) gave an estimation of the crustal structure around the InSight landing site. We computed the diffusivity and scattering quality factor by referring to their supporting materials together with the diffusion model described by Strobach (1970). Consequently, we obtained $Q_s = 100 – 435$ at 0.5 – 2.25 Hz (yellow area in Figure 5b). At the low frequency (< 0.1 Hz), this study provided the first estimation of Q_i and Q_s using the largest marsquake (S1222a) by applying the radiative transfer theory on a spherical Mars (orange area in Figures 5a-b).

7.4 Comparison of three solid bodies

Comparing the Martian Q_i with those of the Earth and the Moon, we found that the absorption feature coincided with the lunar one at the high frequency, whereas it turned into a more Earth-like value at the middle and low frequencies. On the other hand, the Martian scattering quality factor is in accordance with the Earth's lithosphere. These results are consistent with the general marsquake features. The event lasts a few tens of minutes, which is longer than earthquakes but not as long as moonquakes [e.g., Lognonné et al. (2020); Onodera et al. (2022)]. Furthermore, the Martian scattering is not as intense as the Moon, which makes the seismic phases identifiable like earthquakes. According to the quantitative comparison in Figures 5a-b, we can preliminarily conclude that the Martian absorption and scattering properties are more Earth-like rather than Moon-like.

8 Conclusion

In this study, we investigated the properties of seismic scattering and intrinsic absorption on Mars. In previous studies, these parameters were not constrained at frequen-

301 cies below 0.1 Hz. We provided initial estimations of the scattering and intrinsic Q at
 302 that frequency, focusing on the long-lasting surface wave coda observed in the S1222a
 303 marsquake. Using the radiative transfer theory on a spherical Mars, we succeeded in mod-
 304 eling the observed seismic coda features. As a result, we found $Q_i = 1000 - 1500$ and
 305 $Q_s = 30 - 500$, respectively.

306 In the comparison of the Martian quality factors derived so far with other solid bod-
 307 ies, we found that the overall scattering and absorption features of Mars appear simi-
 308 lar to that of the Earth. Because the current estimation is building on only a small por-
 309 tion of the detected marsquakes, we hope that future works will update our results through
 310 more systematic and thorough analyses to better illustrate the heterogeneous structure
 311 inside the red planet.

312 Data availability

313 The SEIS data from the InSight mission used in this study can be retrieved through
 314 InSight Mars SEIS Data Service (2019) and InSight Marsquake Service (2022). A sam-
 315 ple code for downloading data from the IRIS web server can be found at Onodera (2022).

316 Acknowledgments

317 We acknowledge NASA, CNES, their partner agencies and Institutions (UKSA, SSO,
 318 DLR, JPL, IPGP-CNRS, ETHZ, IC, and MPS- MPG), and the flight operations team
 319 at JPL, SISMOC, MSDS, IRIS-DMC, and PDS for acquiring and providing InSight data,
 320 including SEED SEIS data. This is InSight contribution number 313.

321 References

- 322 Aki, K. (1969). Analysis of the seismic coda of local earthquakes as scattered waves.
 323 *Journal of Geophysical Research (1896-1977)*, *74*(2), 615-631. doi: [https://doi](https://doi.org/10.1029/JB074i002p00615)
 324 [.org/10.1029/JB074i002p00615](https://doi.org/10.1029/JB074i002p00615)
- 325 Aki, K., & Chouet, B. (1975). Origin of coda waves: Source, attenuation, and scat-
 326 tering effects. *Journal of Geophysical Research (1896-1977)*, *80*(23), 3322-3342.
 327 doi: <https://doi.org/10.1029/JB080i023p03322>
- 328 Banerdt, W. B., Smrekar, S. E., Banfield, D., Giardini, D., Golombek, M., Johnson,
 329 C. L., ... Wieczorek, M. (2020). Initial results from the insight mission on
 330 mars. *Nature Geoscience*, *13*(3), 183-189. doi: [10.1038/s41561-020-0544-y](https://doi.org/10.1038/s41561-020-0544-y)
- 331 Blanchette-Guertin, J.-F., Johnson, C. L., & Lawrence, J. F. (2012). Investigation
 332 of scattering in lunar seismic coda. *Journal of Geophysical Research: Planets*,
 333 *117*(E6). doi: <https://doi.org/10.1029/2011JE004042>
- 334 Dziewonski, A. M., & Anderson, D. L. (1981). Preliminary reference earth model.
 335 *Physics of the Earth and Planetary Interiors*, *25*(4), 297-356. doi: [https://doi](https://doi.org/10.1016/0031-9201(81)90046-7)
 336 [.org/10.1016/0031-9201\(81\)90046-7](https://doi.org/10.1016/0031-9201(81)90046-7)
- 337 Garcia, R. F., Daubar, I. J., Beucler, É., Posiolova, L. V., Collins, G. S., Lognonné,
 338 P., ... Banerdt, W. B. (2022). Newly formed craters on mars located using
 339 seismic and acoustic wave data from insight. *Nature Geoscience*, *15*(10),
 340 774-780. doi: [10.1038/s41561-022-01014-0](https://doi.org/10.1038/s41561-022-01014-0)
- 341 Giardini, D., Lognonné, P., Banerdt, W. B., Pike, W. T., Christensen, U., Ceylan,
 342 S., ... Yana, C. (2020). The seismicity of mars. *Nature Geoscience*, *13*,
 343 205-212. doi: [10.1038/s41561-020-0539-8](https://doi.org/10.1038/s41561-020-0539-8)
- 344 Gillet, K., Margerin, L., Calvet, M., & Monnerneau, M. (2017). Scattering at-
 345 tenuation profile of the moon: Implications for shallow moonquakes and the
 346 structure of the megaregolith. *Physics of the Earth and Planetary Interiors*,
 347 *262*, 28-40. doi: <https://doi.org/10.1016/j.pepi.2016.11.001>
- 348 Golombek, M., Williams, N., Warner, N. H., Parker, T., Williams, M. G., Daubar,

- 349 I., ... Sklyanskiy, E. (2020). Location and setting of the mars insight
 350 lander, instruments, and landing site. *Earth and Space Science*, 7(10),
 351 e2020EA001248. (e2020EA001248 2020EA001248) doi: [https://doi.org/](https://doi.org/10.1029/2020EA001248)
 352 10.1029/2020EA001248
- 353 InSight Mars SEIS Data Service. (2019). *SEIS raw data, InSight mission*. IPGP,
 354 JPL, CNES, ETHZ, ICL, MPS, ISAE-Supaero, LPG, MFSC. doi: 10.18715/
 355 SEIS.INSIGHT.XB_2016
- 356 InSight Marsquake Service. (2022). *Mars Seismic Catalogue, InSight Mission; V12*
 357 *2022-10-01*. ETHZ, IPGP, JPL, ICL, Univ. Bristol. doi: 10.12686/A18
- 358 Karakostas, F., Schmerr, N., Maguire, R., Huang, Q., Kim, D., Lekic, V., ...
 359 Banerdt, B. (2021). Scattering Attenuation of the Martian Interior through
 360 Coda-Wave Analysis. *Bulletin of the Seismological Society of America*, 111(6),
 361 3035-3054. doi: 10.1785/0120210253
- 362 Kawamura, T., Clinton, J. F., Zenhäusern, G., Ceylan, S., Horleston, A. C., Dah-
 363 men, N. L., ... Banerdt, W. B. (2022). S1222a - the largest marsquake
 364 detected by insight. *Geophysical Research Letters*, e2022GL101543. doi:
 365 <https://doi.org/10.1029/2022GL101543>
- 366 Khan, A., Ceylan, S., van Driel, M., Giardini, D., Lognonné, P., Samuel, H., ...
 367 Banerdt, W. B. (2021). Upper mantle structure of mars from insight seismic
 368 data. *Science*, 373(6553), 434-438. doi: 10.1126/science.abf2966
- 369 Kim, D., Banerdt, W. B., Ceylan, S., Giardini, D., Lekić, V., Lognonné, P., ... Pan-
 370 ning, M. P. (2022). Surface waves and crustal structure on mars. *Science*,
 371 378(6618), 417-421. doi: 10.1126/science.abq7157
- 372 Knapmeyer-Endrun, B., Panning, M. P., Bissig, F., Joshi, R., Khan, A., Kim, D., ...
 373 Banerdt, W. B. (2021). Thickness and structure of the martian crust from in-
 374 sight seismic data. *Science*, 373(6553), 438-443. doi: 10.1126/science.abf8966
- 375 Lee, W. S., Sato, H., & Lee, K. (2003). Estimation of s-wave scattering coef-
 376 ficient in the mantle from envelope characteristics before and after the scs
 377 arrival. *Geophysical Research Letters*, 30(24). doi: [https://doi.org/10.1029/](https://doi.org/10.1029/2003GL018413)
 378 2003GL018413
- 379 Lee, W. S., Sato, H., & Lee, K. (2006). Scattering coefficients in the mantle re-
 380 vealed from the seismogram envelope analysis based on the multiple isotropic
 381 scattering model. *Earth and Planetary Science Letters*, 241(3), 888-900. doi:
 382 <https://doi.org/10.1016/j.epsl.2005.10.035>
- 383 Lognonné, P., Banerdt, W. B., Giardini, D., Pike, W. T., Christensen, U.,
 384 Laudet, P., ... Wookey, J. (2019). Seis: Insight's seismic experiment
 385 for internal structure of mars. *Space Science Reviews*, 215(1), 12. doi:
 386 10.1007/s11214-018-0574-6
- 387 Lognonné, P., Banerdt, W. B., Pike, W. T., Giardini, D., Christensen, U., Garcia,
 388 R. F., ... Zweifel, P. (2020). Constraints on the shallow elastic and anelas-
 389 tic structure of mars from insight seismic data. *Nature Geoscience*, 13(3),
 390 213-220. doi: 10.1038/s41561-020-0536-y
- 391 Maeda, T., Sato, H., & Ohtake, M. (2006). Constituents of vertical-component coda
 392 waves at long periods. *pure and applied geophysics*, 163(2), 549-566. doi: 10
 393 .1007/s00024-005-0031-9
- 394 Margerin, L. (2017). Computation of green's function of 3-d radiative transport
 395 equations for non-isotropic scattering of p and unpolarized s waves. *Pure and*
 396 *Applied Geophysics*, 174(11), 4057-4075. doi: 10.1007/s00024-017-1621-z
- 397 Masters, G., Woodhouse, J., & Freeman, G. (2011). *Mineos v1.0.2 [software]*. Com-
 398 putational Infrastructure for Geodynamics.
- 399 Menina, S., Margerin, L., Kawamura, T., Lognonné, P., Marti, J., Drilleau, M.,
 400 ... Banerdt, W. B. (2021). Energy Envelope and Attenuation Characteris-
 401 tics of High-Frequency (HF) and Very-High-Frequency (VF) Martian Events.
 402 *Bulletin of the Seismological Society of America*, 111(6), 3016-3034. doi:
 403 10.1785/0120210127

- 404 Nakamura, Y. (1976). Seismic energy transmission in the lunar surface zone
 405 determined from signals generated by movement of Lunar Rovers. *Bul-*
 406 *letin of the Seismological Society of America*, 66(2), 593-606. doi: 10.1785/
 407 BSSA0660020593
- 408 Onodera, K. (2022). *Access to scientific data obtained by NASA's Mars exploration*
 409 *mission "InSight"*. Researchmap. Retrieved from [https://researchmap.jp/](https://researchmap.jp/blogs/blog_entries/view/809479/d29ec3b7f0fdd5a15a3be04ec97dc762?frame_id=1470639)
 410 [blogs/blog_entries/view/809479/d29ec3b7f0fdd5a15a3be04ec97dc762](https://researchmap.jp/blogs/blog_entries/view/809479/d29ec3b7f0fdd5a15a3be04ec97dc762?frame_id=1470639)
 411 [?frame_id=1470639](https://researchmap.jp/blogs/blog_entries/view/809479/d29ec3b7f0fdd5a15a3be04ec97dc762?frame_id=1470639)
- 412 Onodera, K., Kawamura, T., Tanaka, S., Ishihara, Y., & Maeda, T. (2022). Quan-
 413 titative evaluation of the lunar seismic scattering and comparison between
 414 the Earth, Mars, and the Moon. *Journal of Geophysical Research: Planets*,
 415 e2022JE007558. doi: <https://doi.org/10.1029/2022JE007558>
- 416 Prudencio, J., Del Pezzo, E., Ibáñez, J. M., Giampiccolo, E., & Patané, D.
 417 (2015). Two-dimensional seismic attenuation images of stromboli island
 418 using active data. *Geophysical Research Letters*, 42(6), 1717-1724. doi:
 419 <https://doi.org/10.1002/2015GL063293>
- 420 Sato, H. (1977). Energy propagation including scattering effects sengl isotropic
 421 scattering approximation. *Journal of Physics of the Earth*, 25(1), 27-41. doi:
 422 10.4294/jpe1952.25.27
- 423 Sato, H. (2019). Isotropic scattering coefficient of the solid earth. *Geophysical Jour-*
 424 *nal International*, 218(3), 2079-2088. doi: 10.1093/gji/ggz266
- 425 Sato, H., Fehler, M. C., & Maeda, T. (2012). *Seismic wave propagation and scat-*
 426 *tering in the heterogeneous earth: Second edition*. Springer Berlin, Heidelberg.
 427 doi: 10.1007/978-3-642-23029-5
- 428 Sato, H., & Nishino, M. (2002). Multiple isotropic-scattering model on the
 429 spherical earth for the synthesis of rayleigh-wave envelopes. *Journal of*
 430 *Geophysical Research: Solid Earth*, 107(B12), ESE 7-1-ESE 7-9. doi:
 431 <https://doi.org/10.1029/2001JB000915>
- 432 Sato, H., & Nohechi, M. (2001). Envelope formation of long-period rayleigh waves in
 433 vertical component seismograms: Single isotropic scattering model. *Journal of*
 434 *Geophysical Research: Solid Earth*, 106(B4), 6589-6594. doi: [https://doi.org/](https://doi.org/10.1029/2000JB900383)
 435 [10.1029/2000JB900383](https://doi.org/10.1029/2000JB900383)
- 436 Scholz, J.-R., Widmer-Schmidrig, R., Davis, P., Lognonné, P., Pinot, B., Garcia,
 437 R. F., ... Banerdt, W. B. (2020). Detection, analysis, and removal of
 438 glitches from insight's seismic data from mars. *Earth and Space Science*,
 439 7(11), e2020EA001317. (e2020EA001317 10.1029/2020EA001317) doi:
 440 <https://doi.org/10.1029/2020EA001317>
- 441 Strobach, K. (1970). Scattering of seismic waves and lunar seismograms. *J. Geo-*
 442 *phys.*, 36, 643-645.
- 443 Stähler, S. C., Khan, A., Banerdt, W. B., Lognonné, P., Giardini, D., Ceylan, S.,
 444 ... Smrekar, S. E. (2021). Seismic detection of the martian core. *Science*,
 445 373(6553), 443-448. doi: 10.1126/science.abi7730
- 446 Wegler, U. (2003). Analysis of multiple scattering at vesuvius volcano, italy,
 447 using data of the tomoves active seismic experiment. *Journal of Vol-*
 448 *canology and Geothermal Research*, 128(1), 45-63. (Putting Volcano
 449 Seismology in a Physical Context. In memory of Bruno Martinelli) doi:
 450 [https://doi.org/10.1016/S0377-0273\(03\)00246-4](https://doi.org/10.1016/S0377-0273(03)00246-4)
- 451 Wu, R.-S. (1985). Multiple scattering and energy transfer of seismic waves —
 452 separation of scattering effect from intrinsic attenuation — I. Theoretical mod-
 453 elling. *Geophysical Journal International*, 82(1), 57-80.
- 454 Yamamoto, M., & Sato, H. (2010). Multiple scattering and mode conversion re-
 455 vealed by an active seismic experiment at asama volcano, japan. *Journal of*
 456 *Geophysical Research: Solid Earth*, 115(B7). doi: [https://doi.org/10.1029/](https://doi.org/10.1029/2009JB007109)
 457 [2009JB007109](https://doi.org/10.1029/2009JB007109)
- 458 Yoshimoto, K., & Jin, A. (2008). Chapter 10 coda energy distribution and attenu-

459

ation. In *Earth heterogeneity and scattering effects on seismic waves* (Vol. 50,
p. 265-299). Elsevier. doi: [https://doi.org/10.1016/S0065-2687\(08\)00010-1](https://doi.org/10.1016/S0065-2687(08)00010-1)

460

Figure1.

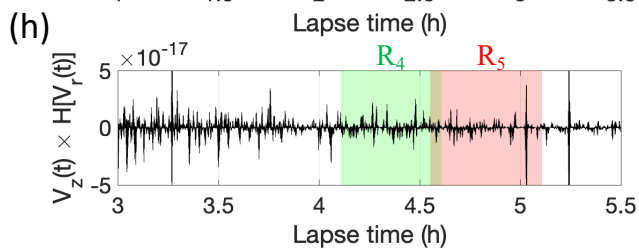
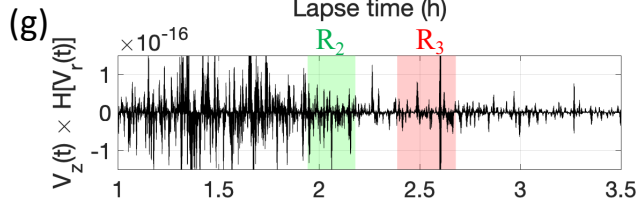
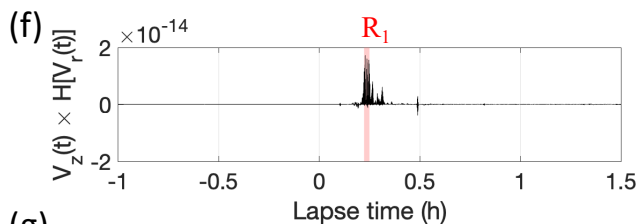
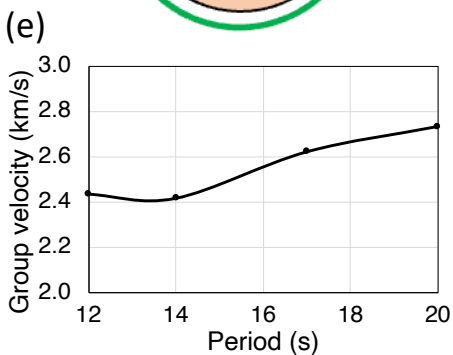
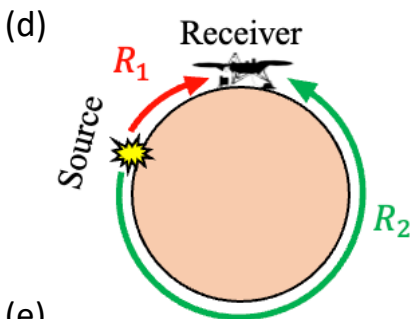
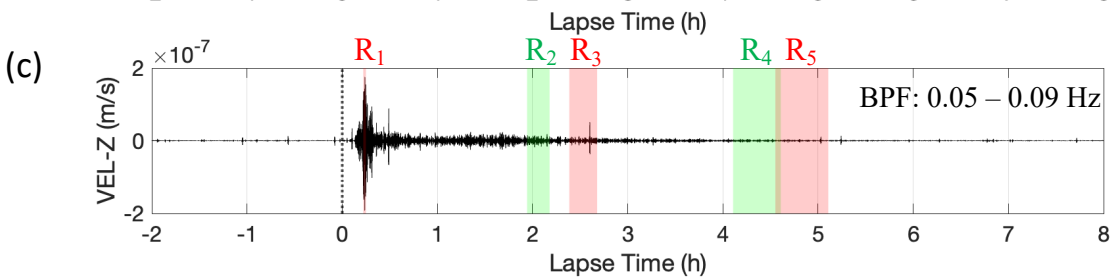
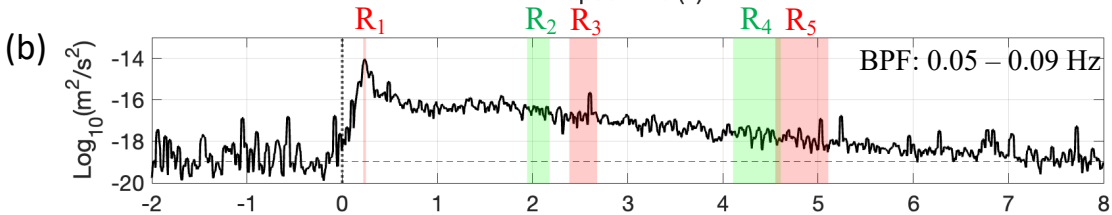
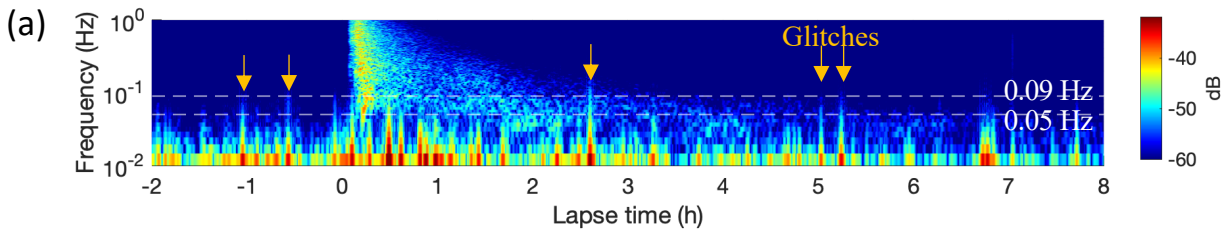
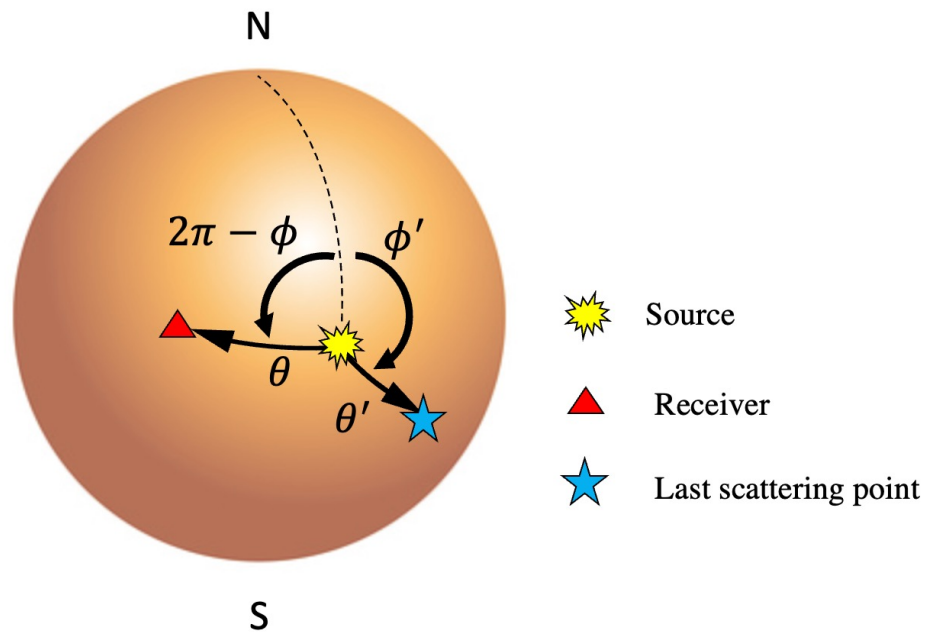
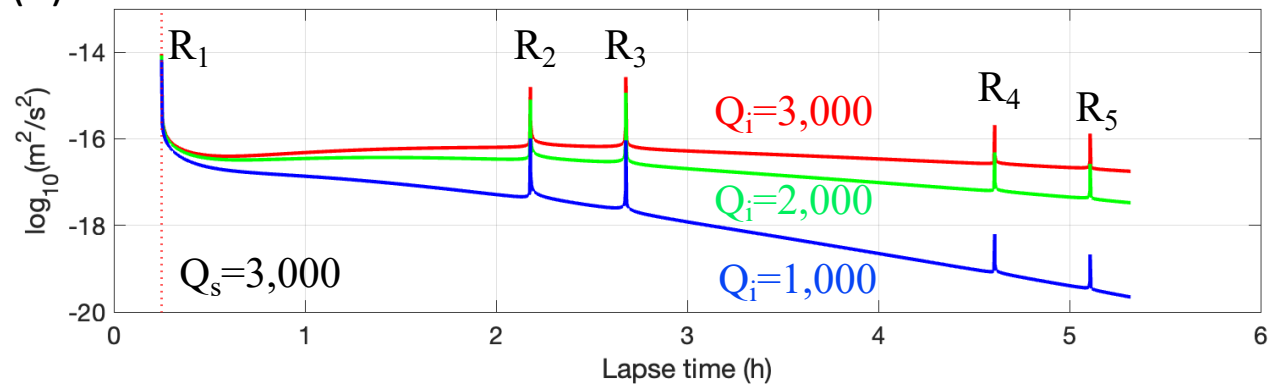


Figure2.

(a)



(b)



(c)

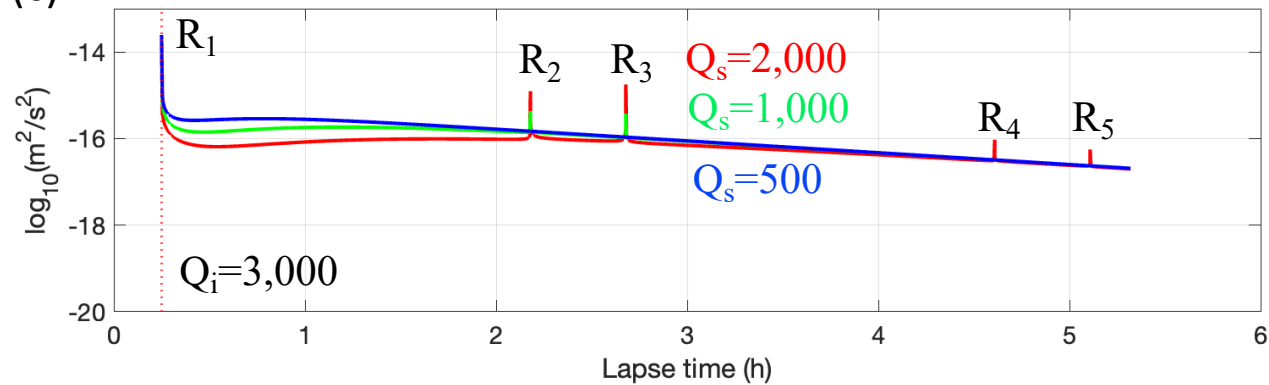


Figure3.

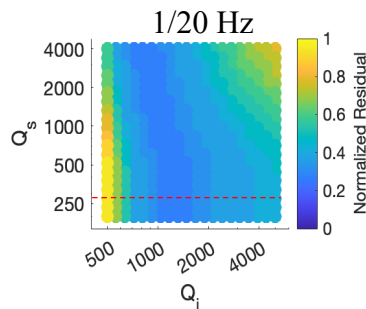
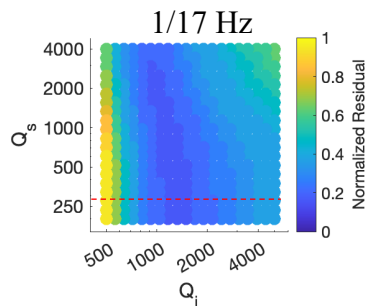
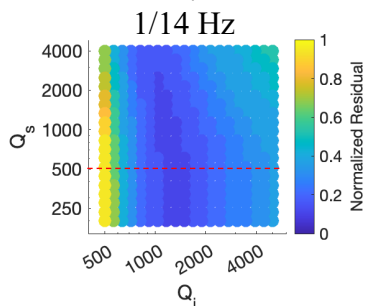
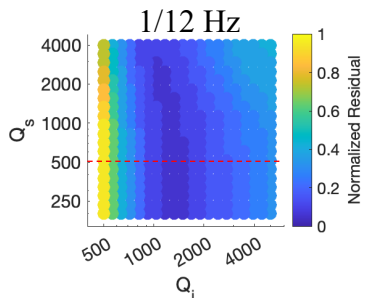
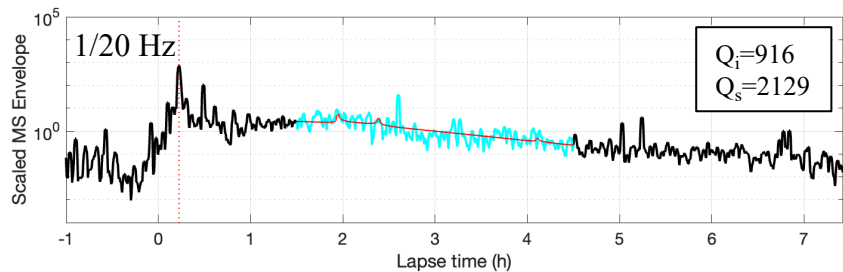
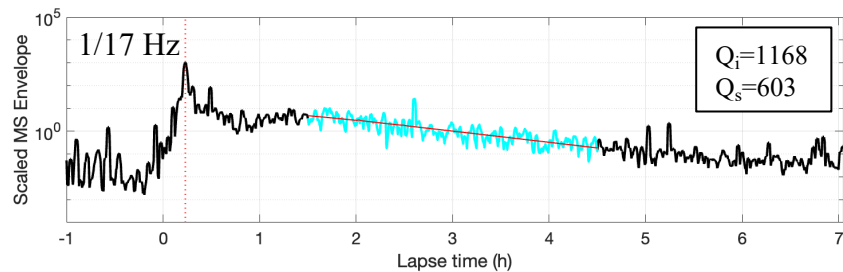
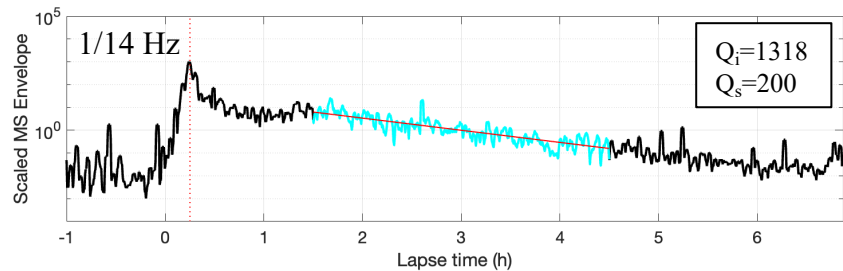
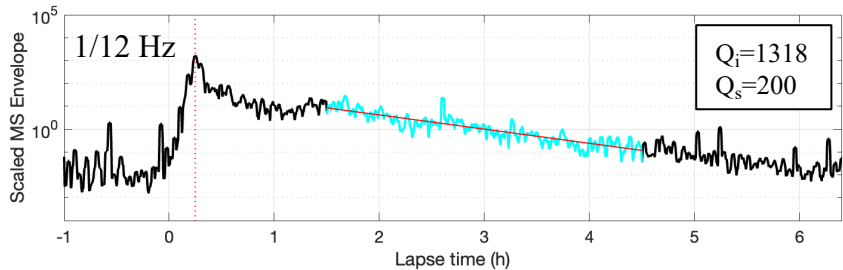
(a) Residual map**(b) Best-fitted curve**

Figure4.

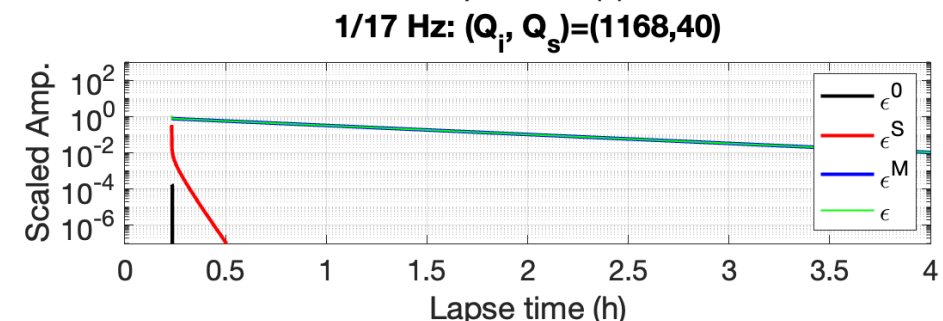
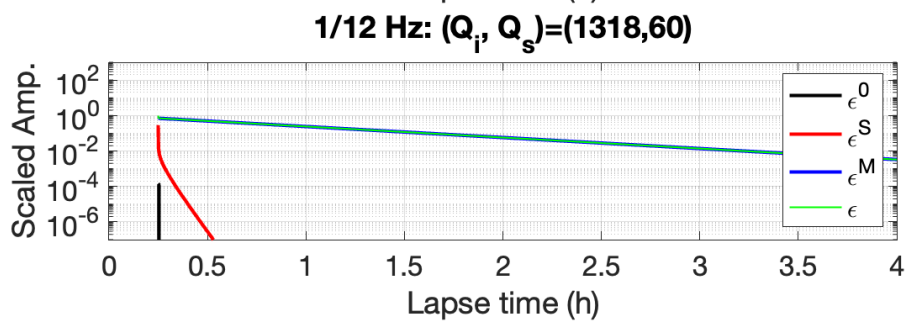
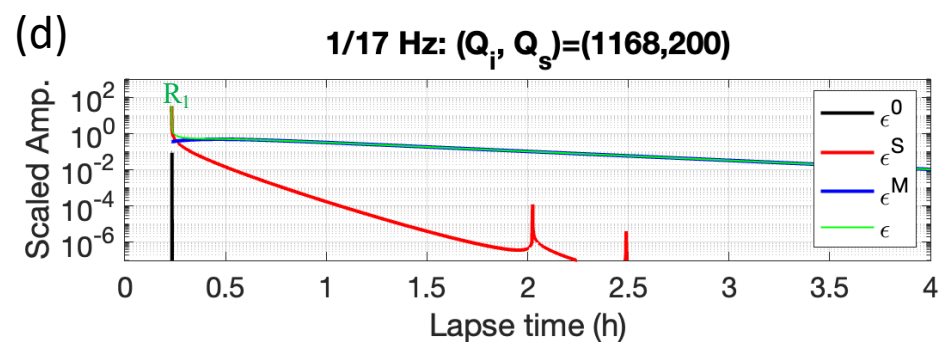
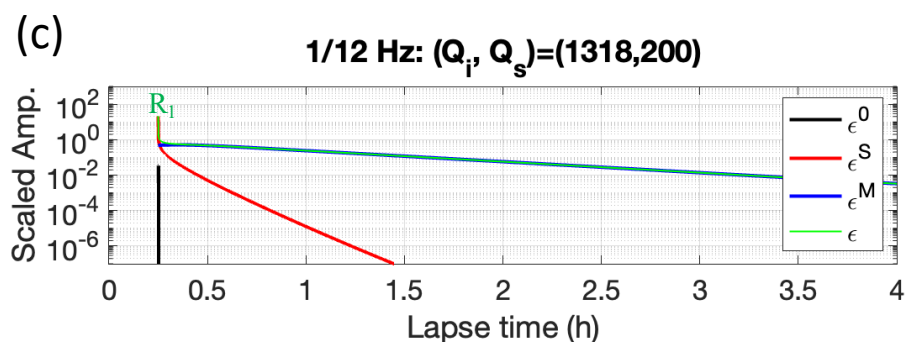
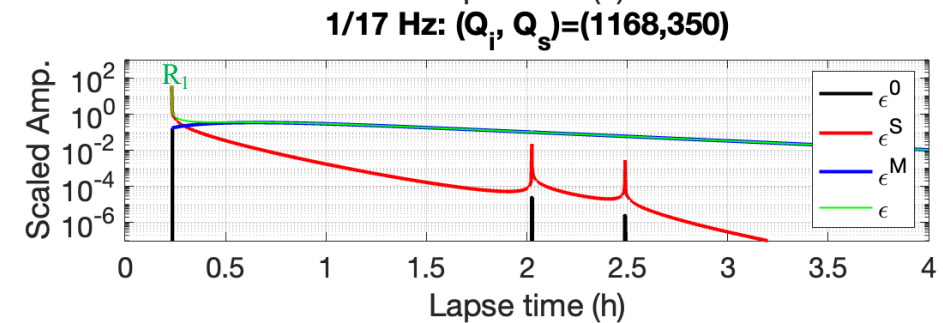
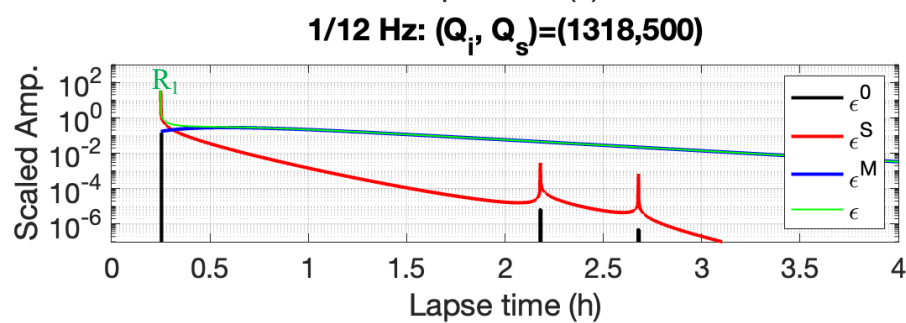
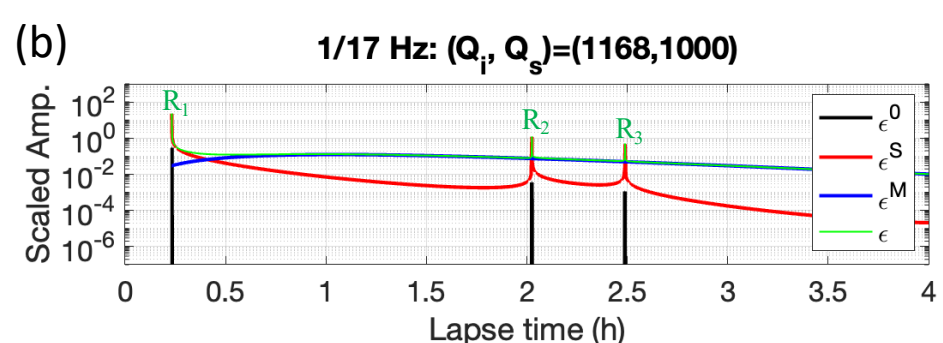
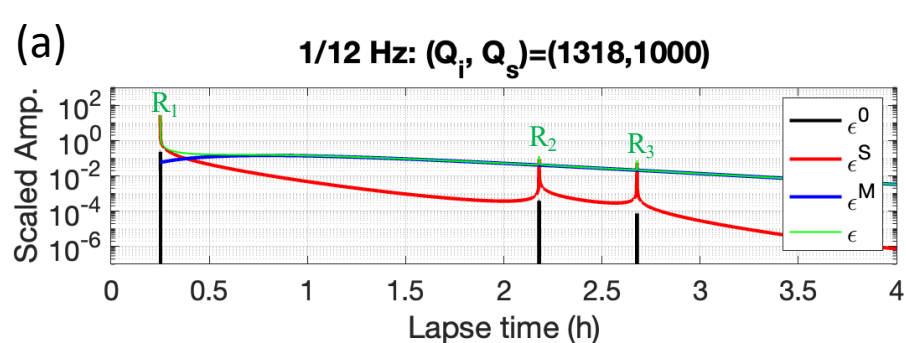
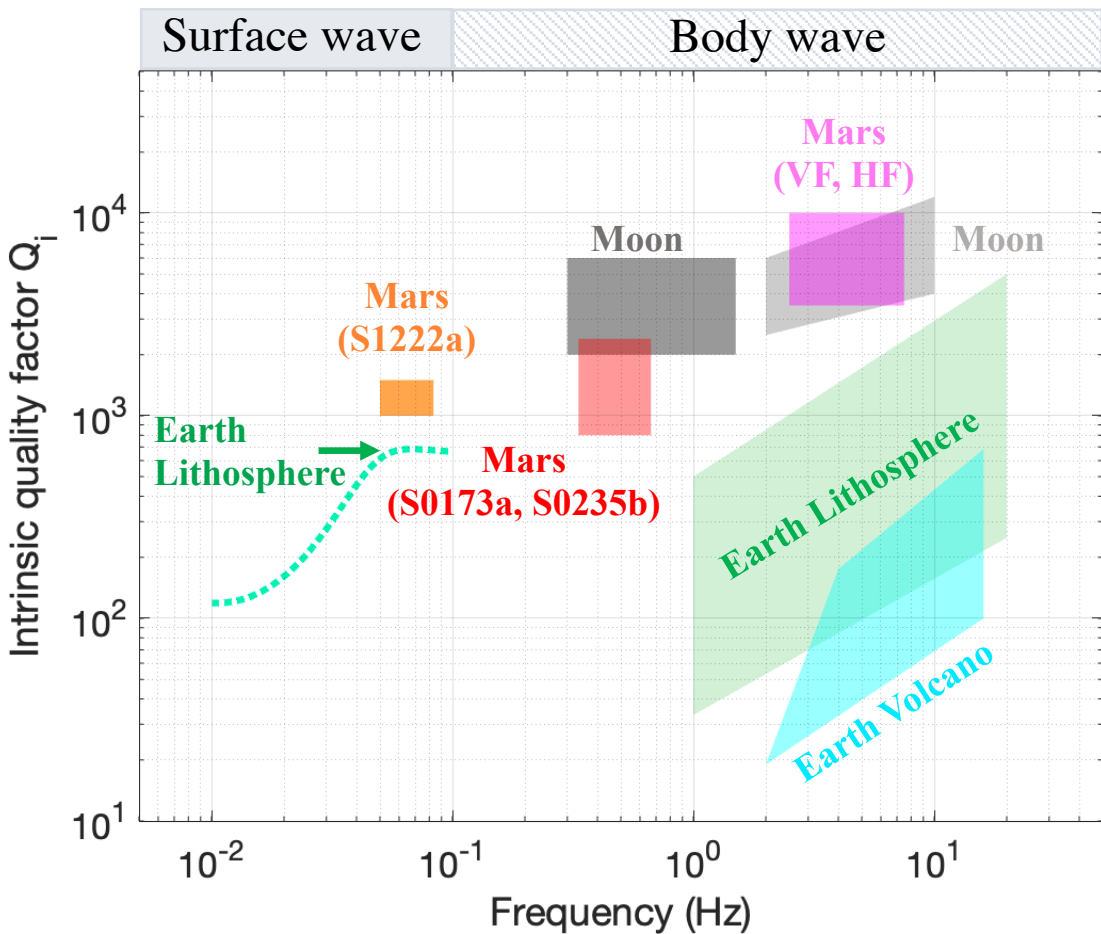
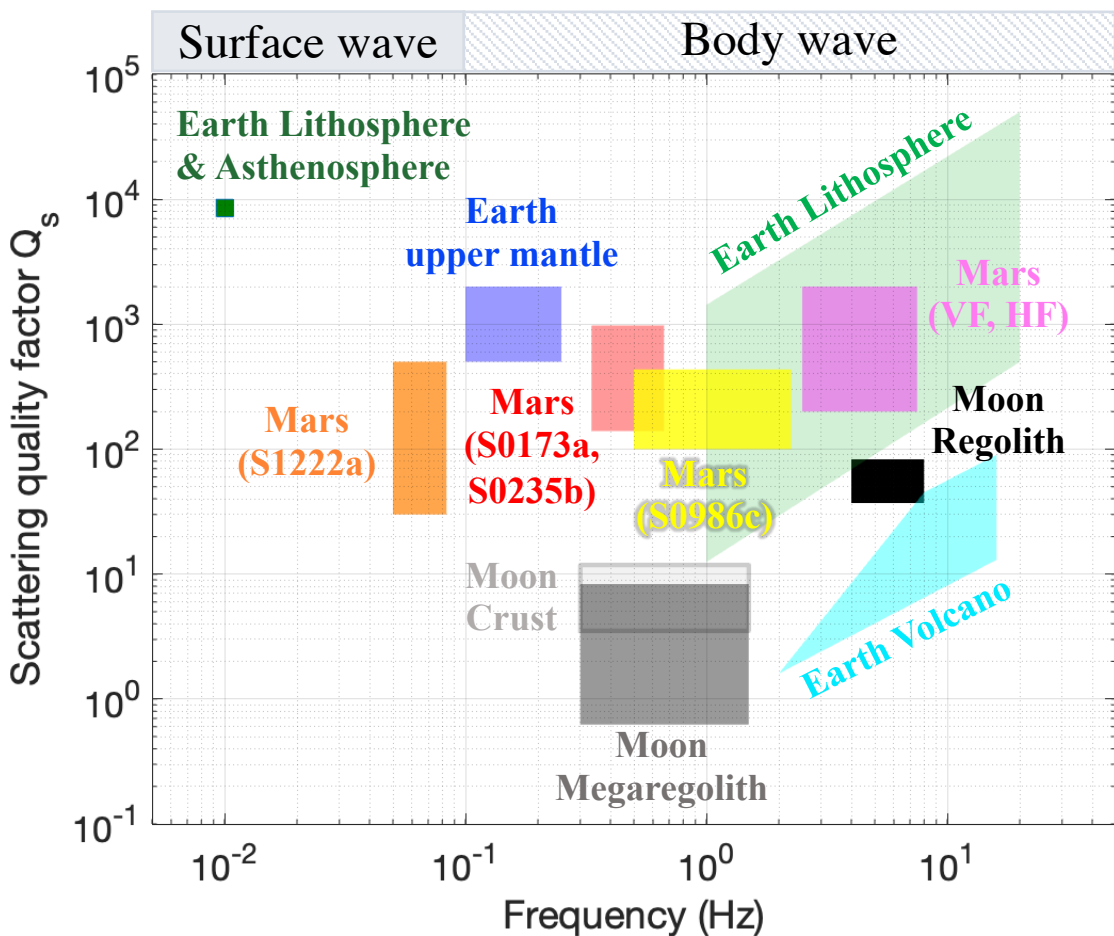


Figure 5.

(a)



(b)



**Seismic scattering and absorption properties of Mars
estimated through coda analysis on a long-period
surface wave of S1222a marsquake**

Keisuke Onodera¹, Takuto Maeda², Kiwamu Nishida¹, Taichi Kawamura³,

Sabrina Menina³, Ludovic Margerin⁴, Philippe Lognonné³, William Bruce Barnerdt⁵

¹Earthquake Research Institute, The University of Tokyo, Tokyo, Japan

²Hirosaki University, Aomori, Japan

³Institut de Physique du Globe de Paris, Université Paris Cité, CNRS, Paris, France

⁴Institut de Recherche en Astrophysique et Planétologie, Université Toulouse III, CNRS, CNES, Toulouse, France.

⁵Jet Propulsion Laboratory, California Institute of Technology, California, USA

Contents of this file

Figures S1 to S4

Introduction

This document includes the information, which is not included in the main text, to help readers better understand our study. In the following document, we present three supporting figures related to (1) the background noise level, (2) theoretical curves related to grid search in the main text, (3) constraining Q_s , and (4) the scaled energy factor. These topics are related to the description in Section 1 and 6 in the main text.

Supporting Figures S1 – S4

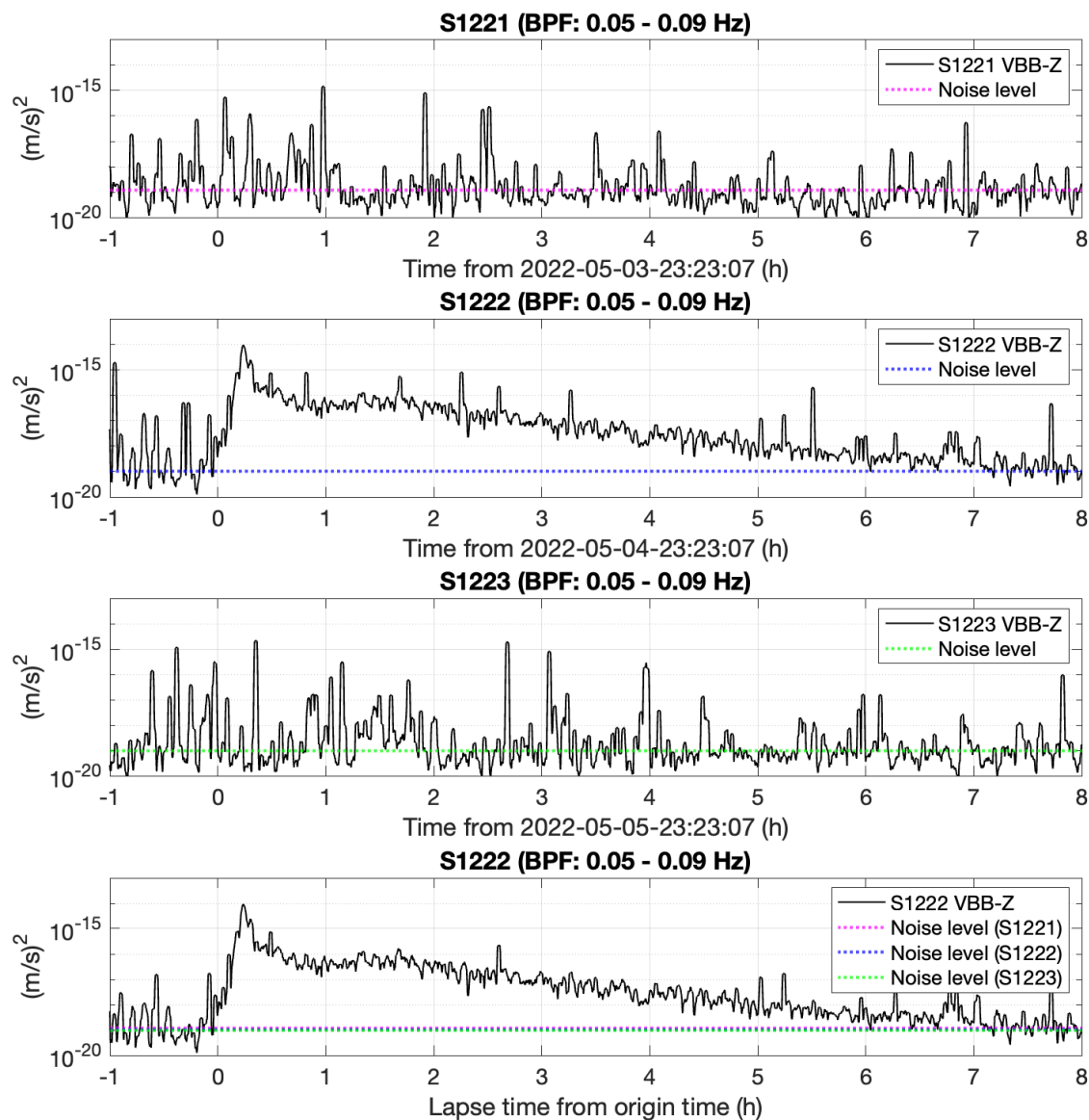


Figure S1. Comparison of noise level between Sol1221, Sol1222, and Sol1223. The top three figures show the vertical mean squared (MS) envelopes (black) and the noise levels (colored) at each sol. For Sol1221 and S1223, the noise level was estimated with the median value for the nine hour time window. Regarding Sol1222, the noise level was estimated using the time window before the origin time (< 0 h). The bottom figure compares the noise levels on Sol1221, Sol1222, and Sol1223. The black profile is the deglitched MS envelope on S1222 including S1222a marsquake.

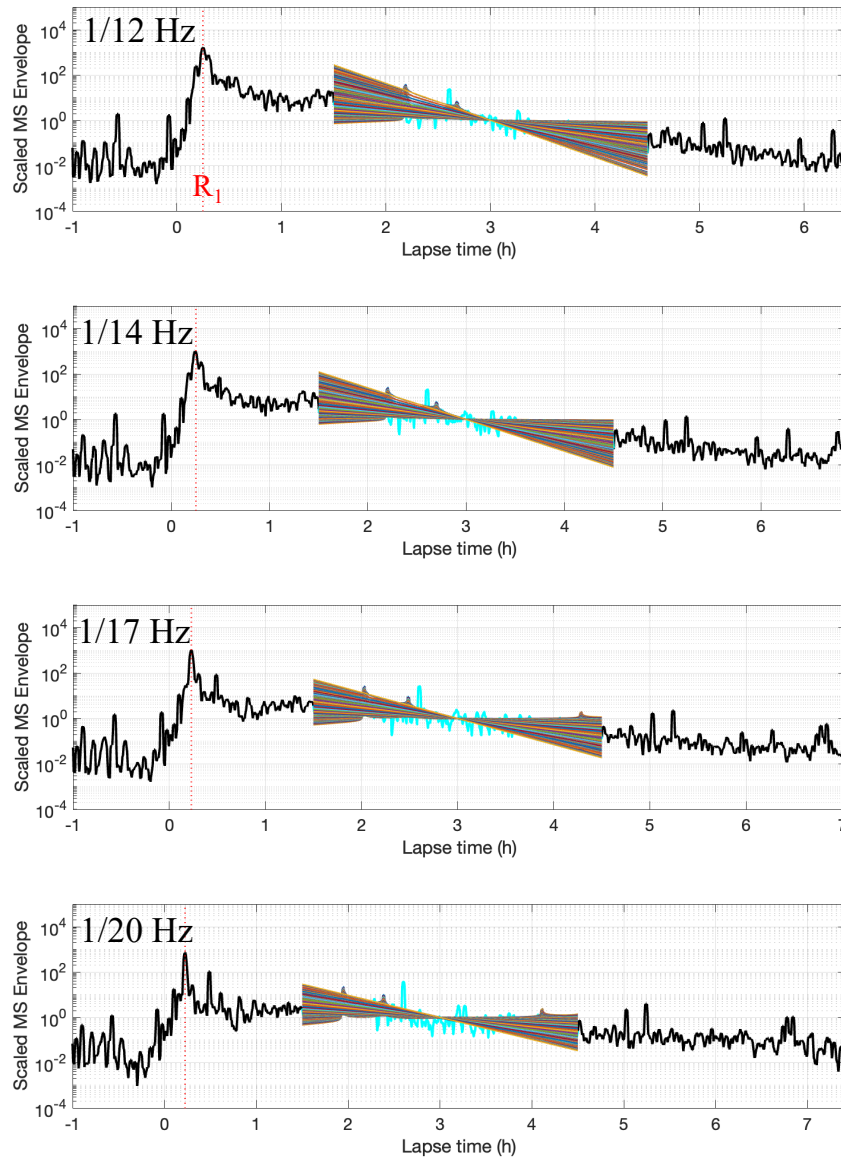


Figure S2. Representation of all of the calculated theoretical curves (colored) superposed on the observed MS envelope (black and cyan). For the fitting, the MS envelope for the time window of 1.5 – 3.5 h was used. The amplitude is scaled with the average amplitude between 1.5 – 3.5 h time window. The red dotted line shows the R_1 arrival.

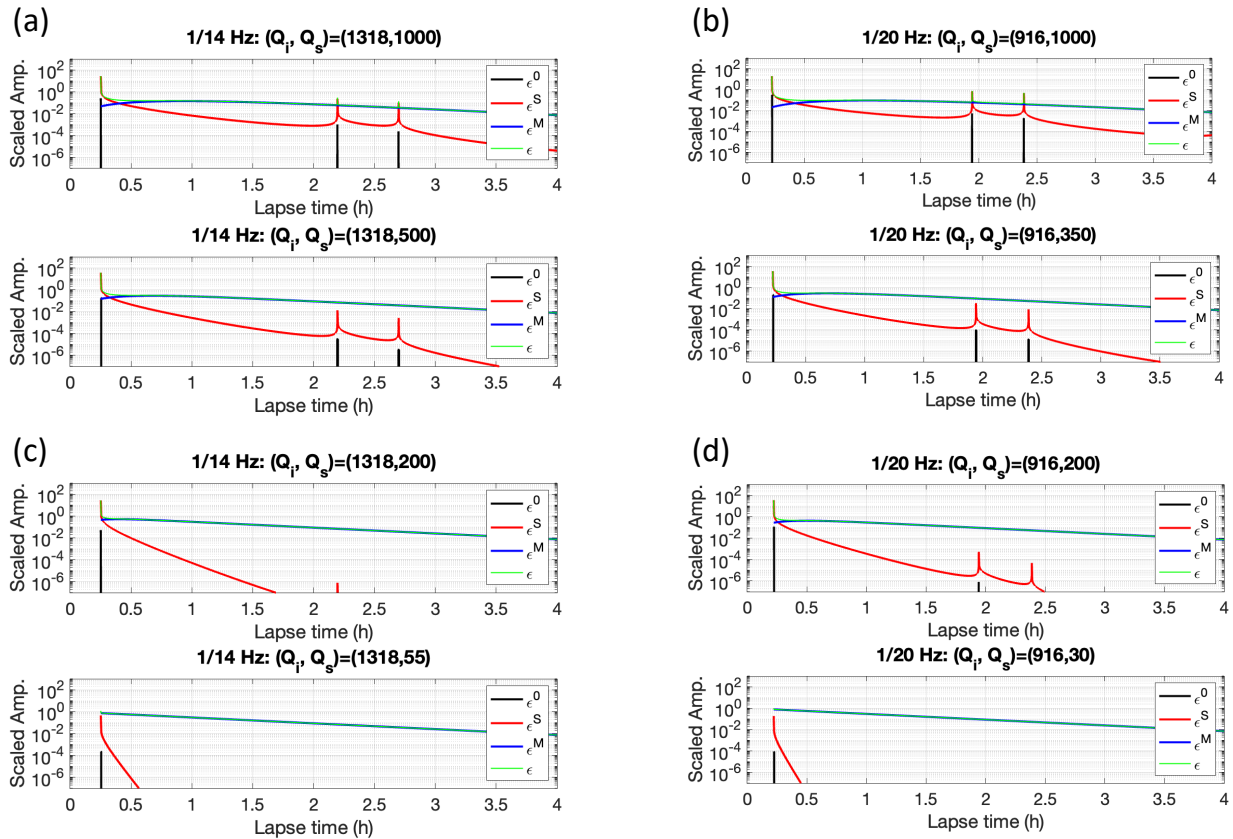


Figure S3. (a)-(b) Examples of parameter study results to estimate the upper limit of Q_s at 1/14 Hz and 1/20 Hz. The black lines are the direct wave component, the red profile is the single-scattered component, the blue is the multiple-scattered component, and the green is the convolved profile. The first row is for $Q_s = 1000$, where the multi-orbital phases are clearly seen (e.g., R_2 and R_3). The second row is the case for the upper limit of Q_s , where the contribution of the multiple scattering is strong enough to bury the multi-orbital phases. **(c)-(d)** Examples of parameter study results to estimate the lower limit of Q_s at 1/14 Hz and 1/20 Hz. The first row is for $Q_s = 200$, where the R_1 phase is clearly seen. The second row is the case for the lower limit of Q_s , where the contribution of the multiple scattering is strong enough to bury the R_1 phase.

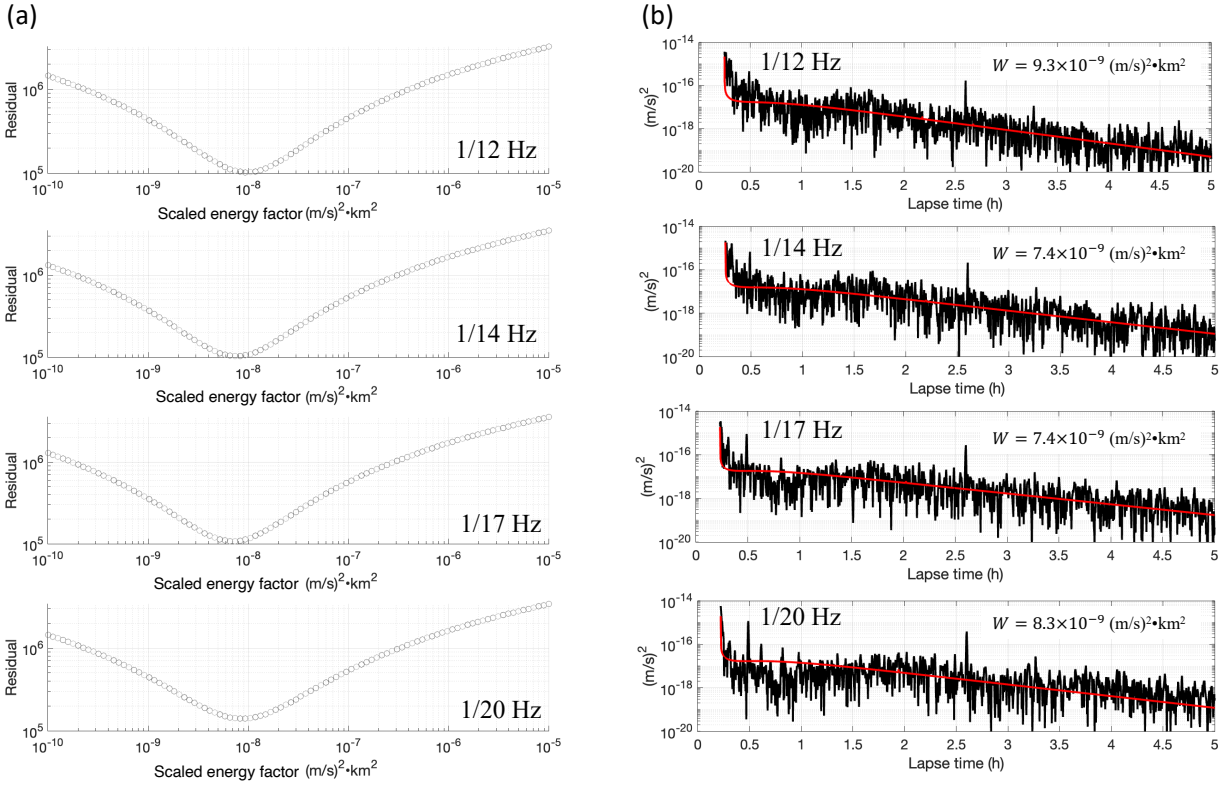


Figure S4. (a) Trace of the residual with the scaled energy factor. The summation of residual was calculated for each scaled energy factor in the same manner as Equation 8 in the main text. In that calculation, Q_i for each frequency band was fixed to the best-fitted value presented in Figure 3 in the main text, and Q_s was fixed to the upper limit that is described in Section 6 in the main text. **(b)** Comparison of the best-fitted curve (red) and the observed MS envelope (black). The most preferable scaled energy factor for the respective frequency bands is shown in the upper right corner in each panel.